



1

2

3

4

5

6

7

Influence of Stratification and Wind Forcing on the Dynamics of Lagrangian

8

Residual Velocity in a Periodically Stratified Estuary

9

Fangjing Deng¹, Feiyu Jia¹, Rui Shi², Shuwen Zhang¹, Qiang Lian¹, Xiaolong Zong¹,

10

Zhaoyun Chen^{1,*}

11

¹ *Guangdong Provincial Key Laboratory of Marine Disaster Prediction and Prevention, Institute of Marine*

12

Sciences, Shantou University, Shantou, 515063, China

13

² *State Key Laboratory of Tropical Oceanography, South China Sea Institute of Oceanology, Chinese Academy*

14

of Sciences, Guangzhou, China

15

16

17

18

Correspondence to: Zhaoyun Chen (chenzy@stu.edu.cn)

19

20

21



22 **Abstract**

23 Wind and stratification play pivotal roles in shaping the structure of the Lagrangian
24 residual velocity (LRV). However, the intricate dynamics by which wind and stratification
25 modify the LRV remain poorly studied. This study derives numerical solutions of LRV
26 components and eddy viscosity subcomponents to elucidate the dynamics within the
27 periodically stratified Pearl River estuary. The vertical shear cross-estuary LRV (u_L) is
28 principally governed by the interplay among the eddy viscosity component (u_{Ltu}), the barotropic
29 component (u_{Lba}), and the baroclinic component (u_{Lgr}) under stratified conditions. During neap
30 tides, southwesterly winds notably impact u_L by escalating u_{Ltu} by an order of magnitude within
31 the upper layer. This transforms the eastward flow dominated by u_{Ltu} under wind influence into
32 a westward flow dominated by u_{Lba} in upper shoal regions without wind forcing. The along-
33 estuary LRV exhibits a gravitational circulation characterized by upper-layer outflow
34 engendered by barotropic component (v_{Lba}) and lower-layer inflow predominantly driven by
35 baroclinic component (v_{Lgr}). The presence of southwesterly winds suppresses along-estuary
36 gravitational circulation by diminishing the magnitude of v_{Lba} and v_{Lgr} . The contributions of
37 v_{Lba} and v_{Lgr} are approximately equal, while the ratio between u_{Lba} and u_{Lgr} (u_{Ltu}) fluctuates
38 within the range of 1 to 2 in stratified waters. Under unstratified conditions, LRV exhibits a
39 lateral shear structure due to differing dominant components compared to stratified conditions.
40 In stratified scenarios, the eddy viscosity component of LRV is predominantly governed by the
41 turbulent mean component, while it succumbs to the influence of the tidal straining component
42 in unstratified waters.

43



44 **1. Introduction**

45 Tidal currents are the principal movement in shallow seas and estuaries. However, tidal
46 oscillations are not the predominant factor regarding the long-term transport of mass, such as
47 pollutants, sediments, nutrients, and suspended materials. Instead, residual current, which
48 remains after filtering out tidal movements, plays a crucial role in long-term mass transport.
49 Therefore, unveiling the dynamic mechanisms governing the structure and magnitude of the
50 residual current becomes particularly significant for a correct understanding of the circulation
51 and long-term mass transport in shallow seas and estuaries.

52 Pritchard (1952) proposed a conceptual model of estuarine circulation characterized by a
53 two-layer structure, drawing from extensive observations. A subsequent study by Pritchard
54 (1956) emphasized the crucial role of the horizontal density gradient as the primary driving
55 force for estuarine circulation. Subsequently, the theory of estuarine gravitational circulation
56 was developed, assuming a constant eddy viscosity (Hansen and Rattray, 1965). Nevertheless,
57 it is imperative to acknowledge that estuarine circulation is influenced not solely by density
58 gradients but also by factors such as wind, tides, and other dynamic forces. These external
59 factors possess the ability to modify or even reverse the structure of gravity circulation within
60 estuaries.

61 Several studies have highlighted the significant impact of tidal straining on Eulerian
62 residual velocity (ERV) (Becherer et al., 2011; Monismith et al., 1996). Jay and Musiak (1994)
63 found the ERV induced by tidal straining is comparable to gravitational circulation.
64 Additionally, tidal straining contributes twice as much to the ERV as gravitational circulation
65 without consideration of river runoff (Burchard and Hetland, 2010). The flow induced by tidal
66 straining varies in estuaries with different stratified conditions. When the horizontal density
67 gradient is small, tidal straining dominates the structure of the ERV (Burchard et al., 2011).
68 Cheng et al. (2011) showed that tidal straining induces a typical two-layer circulation in weakly



69 stratified estuaries, while the circulation exhibits a vertical three-layer structure with inflow in
70 the upper and lower layer and outflow in the middle layer in partially and strong stratified
71 estuaries. As stratification intensifies, the ratio of flow induced by tidal straining to
72 gravitational circulation decreases. In a weakly stratified short estuary, tidal straining plays a
73 secondary role in ERV compared to gravitational circulation (Wei et al., 2021). Geyer and
74 MacCready (2014) indicated that the Eulerian mean method tends to overestimate the
75 contribution of tidal straining. Therefore, it is more reasonable to analyze dynamical
76 mechanisms for residual current from the perspective of the Lagrangian tidally averaged theory.

77 In addition to tides and density gradients, wind also plays a significant role in influencing
78 estuarine residual currents and stratification (Verspecht et al., 2009; Jongbloed et al., 2022).
79 Burchard (2009) highlighted that upstream winds weaken stratification and reduce the
80 magnitude of the ERV, whereas the downstream wind sheds the opposite effect. To quantify
81 the destratification effect of upstream wind, Lange and Burchard (2019) introduced the
82 Wedderburn number to analyze the relationship between upstream wind and density gradient.
83 The wind is less inclined to affect the residual current with large Wedderburn numbers and may
84 inhibit gravitational circulation, whereas the structure of ERV reverses with small Wedderburn
85 numbers.

86 While the Eulerian mean method is commonly employed to study estuarine dynamics,
87 there are certain terms within the momentum and mass transport equations that lack clear
88 physical explanations (Ianniello, 1977; Feng et al., 1984). According to Lamb (1975), any flow
89 field must adhere to the principle of mass conservation. In this regard, the Lagrangian residual
90 velocity (LRV) is derived based on the fundamental nature of physical motion, ensuring
91 material conservation and providing an accurate description of circulation in shallow seas
92 (Feng, 1987; Jiang and Feng, 2014).

93 The influence of LRV in semi-closed estuaries and bays affected by tides has received



94 attention from oceanographers (Deng et al., 2019; Jiang and Feng, 2011; Winant, 2008). Quan
95 et al. (2014) employed a numerical model to investigate the impact of the ratio of tidal
96 amplitude to water depth on LRV, and Jiang and Feng (2014) explored how the ratio of estuary
97 length to wavelength affects LRV. Wang et al. (2010) examined the effects of wind, density
98 gradient, and river runoff on LRV using a numerical model. However, this study aims to
99 illustrate structural and magnitudinal variations of the total LRV under different factors,
100 without delving into the underlying dynamic mechanisms. Liu et al. (2021) demonstrated that
101 the influence of wind and density gradients on LRV is closely associated with the initial tidal
102 phase based on the momentum equations, but the specific contribution of each dynamic
103 component to LRV remains poorly studied.

104 Jiang and Feng (2014) explored the dynamical mechanisms for the LRV, which gives to
105 the assumptions of a constant eddy viscosity and linear bottom friction in the entire estuarine.
106 Subsequently, numerical models were utilized to study the contribution of tidal body force to
107 LRV under a constant eddy viscosity, revealing that the Stokes' drift component plays a
108 dominant role (Cui et al., 2019). Chen et al. (2020) analyzed the contribution of each dynamical
109 term to the LRV and found the Stokes' drift component is the dominant component under the
110 condition of the horizontal unvaried but depth-varying eddy viscosity. The above studies are
111 all carried out under a temporally constant eddy viscosity. The impact of spatially varying eddy
112 viscosity on LRV was examined in a narrow model, revealing that nonlinearity leads to a more
113 complex LRV structure (Deng et al., 2017). However, these studies lack a quantitative analysis
114 of the underlying dynamical mechanism. Sheng et al. (2022) demonstrated that the structure of
115 LRV is primarily determined by the combined effects of the barotropic pressure gradient and
116 tidal body force when only barotropic conditions are considered. Deng et al. (2022) further
117 quantitatively analyzed the contributions of each driving force to LRV, considering both
118 temporal and spatial variations in eddy viscosity under a constant density gradient. However,



119 the roles of wind and stratification in LRV dynamics remain poorly studied.

120 The Pearl River, as the third largest river in China, encompasses a complex hydrodynamic
121 environment. The Pearl River estuary (PRE) is a trumpet-like estuary characterized by two
122 deep channels and shallow shoals. In recent years, researchers have increasingly focused on
123 topics such as tidal currents, salinity intrusion, river plume dynamics, and residual current in
124 the PRE (e.g., Gong et al., 2018; Pan et al., 2020; Wei et al., 2022). The estuary displays a
125 typical two-layer circulation as observed in micro-tidal estuaries (Xue et al., 2001). Wang (2014)
126 investigated the temporal and spatial variations of the ERV and analyzed its underlying
127 dynamical mechanisms within the PRE. Lai et al. (2018) discussed the influence of tides and
128 winds on the ERV and the associated dynamical processes using the Eulerian mean momentum
129 equation. Additionally, the nonlinear advection term was identified as an important factor in
130 the ERV within the PRE (Xu et al., 2021). While Chu et al. (2022) explored the hydrodynamic
131 processes and connectivity of the circulation within the estuary from a Lagrangian tidally
132 averaged perspective, a detailed dynamical analysis was not provided. Few studies have
133 focused on the LRV within the PRE, especially regarding its underlying dynamical mechanisms.

134 Analytical solutions regarding the dynamics of LRV are constrained to a temporally
135 constant eddy viscosity, while numerical solutions of LRV's dynamic components disregard
136 the influence of stratification and wind. Consequently, the impact of wind and stratification on
137 LRV dynamics remains enigmatic. Numerical solutions for LRV components are derived to
138 grasp the modifications induced by wind and stratification within each LRV component,
139 ultimately leading to changes in the overall LRV. Furthermore, wind and stratification influence
140 turbulent mixing, subsequently affecting the LRV driven by the eddy viscosity term. Although
141 scholars have extensively examined tidal straining effects on estuarine circulation via the
142 Eulerian mean theory, the analysis of turbulent influences from the Lagrangian mean theory
143 perspective yields distinctions from the Eulerian approach. To illuminate the mechanisms



144 underlying the eddy viscosity component of LRV, we initiate by decomposing this component
145 into four subcomponents. This study pursues two principal objectives: 1) to delve into the
146 mechanisms by which wind and stratification modify LRV components, and 2) to investigate
147 the roles of wind and stratification in the dominant contributor of the eddy viscosity component.
148 This paper will provide valuable insights into the dynamic processes of longitudinal and lateral
149 estuarine circulation based on Lagrangian mean theory under the influence of wind and
150 stratification. These aspects have not been quantitatively assessed in previous studies.
151 Additionally, the proposed decomposition theory of the eddy viscosity component offers a
152 novel approach for analyzing the dominant mechanisms of turbulent components. This paper
153 is structured as follows: Section 2 provides a delineation of model setup parameters, model
154 validation, and LRV decomposition methods. Section 3 outlines the contribution of each
155 component to the overall LRV and the contribution of each subcomponent to the total eddy
156 viscosity component of LRV. The discussion and conclusions are presented in Section 4.

157 **2. Theory and model description**

158 **2.1 The decomposition method**

159 The LRV is decomposed into seven components, including the local acceleration
160 component (u_{Lac} and v_{Lac}), horizontal nonlinear advection component (u_{Ladh} and v_{Ladh}), vertical
161 nonlinear advection component (u_{Ladv} and v_{Ladv}), barotropic pressure gradient component
162 (barotropic component; u_{Lba} and v_{Lba}), baroclinic pressure gradient component (baroclinic
163 component; u_{Lgr} and v_{Lgr}), eddy viscosity component (u_{Ltu} and v_{Ltu}), and horizontal diffusion
164 component (u_{Lho} and v_{Lho}). The detailed decomposition methods are shown in the appendix.
165 Deng et al. (2022) considered a temporally constant density gradient but neglected the effects
166 of periodic stratification and wind forcing. In this paper, one of the primary objectives is to
167 quantify the effects of wind and stratification on the dynamics of the different components of



168 LRV.

169 Wind and stratification play roles in turbulent mixing, which subsequently impacts the
 170 fluctuations of eddy viscosity over a tidal period. This influence extends to the eddy viscosity
 171 component of LRV. To clarify the mechanisms underlying this eddy viscosity component, we
 172 decompose it into four sub-components. We evaluate the distinct contributions of each sub-
 173 component to the total eddy viscosity component, aiming to delve into the dominant dynamic
 174 mechanisms, which is another objective of our paper. The study derives the following
 175 decomposition methods:

$$-\left\langle \frac{1}{D^2} \frac{\partial}{\partial \sigma} \left(v_h \frac{\partial u}{\partial \sigma} \right) \right\rangle / f = -\left\langle \frac{1}{D^2} \frac{\partial}{\partial \sigma} \left(v_{h0} \frac{\partial u_0}{\partial \sigma} \right) \right\rangle / f - \left\langle \frac{1}{D^2} \frac{\partial}{\partial \sigma} \left(v_{h0} \frac{\partial u_1}{\partial \sigma} \right) \right\rangle / f \quad (1)$$

$$-\left\langle \frac{1}{D^2} \frac{\partial}{\partial \sigma} \left(v_{h1} \frac{\partial u_0}{\partial \sigma} \right) \right\rangle / f - \left\langle \frac{1}{D^2} \frac{\partial}{\partial \sigma} \left(v_{h1} \frac{\partial u_1}{\partial \sigma} \right) \right\rangle / f,$$

$$\left\langle \frac{1}{D^2} \frac{\partial}{\partial \sigma} \left(v_h \frac{\partial v}{\partial \sigma} \right) \right\rangle / f = \left\langle \frac{1}{D^2} \frac{\partial}{\partial \sigma} \left(v_{h0} \frac{\partial v_0}{\partial \sigma} \right) \right\rangle / f + \left\langle \frac{1}{D^2} \frac{\partial}{\partial \sigma} \left(v_{h0} \frac{\partial v_1}{\partial \sigma} \right) \right\rangle / f + \quad (2)$$

$$\left\langle \frac{1}{D^2} \frac{\partial}{\partial \sigma} \left(v_{h1} \frac{\partial v_0}{\partial \sigma} \right) \right\rangle / f + \left\langle \frac{1}{D^2} \frac{\partial}{\partial \sigma} \left(v_{h1} \frac{\partial v_1}{\partial \sigma} \right) \right\rangle / f,$$

$$\text{and } u = u_0 + u_1, \quad v = v_0 + v_1, \quad v_h = v_{h0} + v_{h1}, \quad (3)$$

176 where $\langle \rangle$ represents the Lagrangian-averaged operator, u and v are horizontal tidal currents, v_h
 177 is the eddy viscosity, u_l and v_l are tidal average currents, u_0 and v_0 are tidal periodic oscillation
 178 tidal currents, v_{h0} is tidal average eddy viscosity, v_{h1} is tidal periodic oscillation eddy viscosity,
 179 D is time-varying depth, σ is sigma coordinate, and f is Coriolis parameter. The
 180 $-\left\langle \frac{1}{D^2} \frac{\partial}{\partial \sigma} \left(v_{h0} \frac{\partial u_0}{\partial \sigma} \right) \right\rangle / f$ and $\left\langle \frac{1}{D^2} \frac{\partial}{\partial \sigma} \left(v_{h0} \frac{\partial v_0}{\partial \sigma} \right) \right\rangle / f$ represent the coupled component of the tidal-
 181 average eddy viscosity and velocity gradient oscillation (v_{Lk0u0} and u_{Lk0u0}), the
 182 $-\left\langle \frac{1}{D^2} \frac{\partial}{\partial \sigma} \left(v_{h1} \frac{\partial u_0}{\partial \sigma} \right) \right\rangle / f$ and $\left\langle \frac{1}{D^2} \frac{\partial}{\partial \sigma} \left(v_{h1} \frac{\partial v_0}{\partial \sigma} \right) \right\rangle / f$ represent the tidal straining component (v_{Lk1u0}
 183 and u_{Lk1u0}), the $-\left\langle \frac{1}{D^2} \frac{\partial}{\partial \sigma} \left(v_{h0} \frac{\partial u_1}{\partial \sigma} \right) \right\rangle / f$ and $\left\langle \frac{1}{D^2} \frac{\partial}{\partial \sigma} \left(v_{h0} \frac{\partial v_1}{\partial \sigma} \right) \right\rangle / f$ represent the turbulent mean
 184 component (v_{Lk0u1} and u_{Lk0u1}), the $-\left\langle \frac{1}{D^2} \frac{\partial}{\partial \sigma} \left(v_{h1} \frac{\partial u_1}{\partial \sigma} \right) \right\rangle / f$ and $\left\langle \frac{1}{D^2} \frac{\partial}{\partial \sigma} \left(v_{h1} \frac{\partial v_1}{\partial \sigma} \right) \right\rangle / f$ represent the

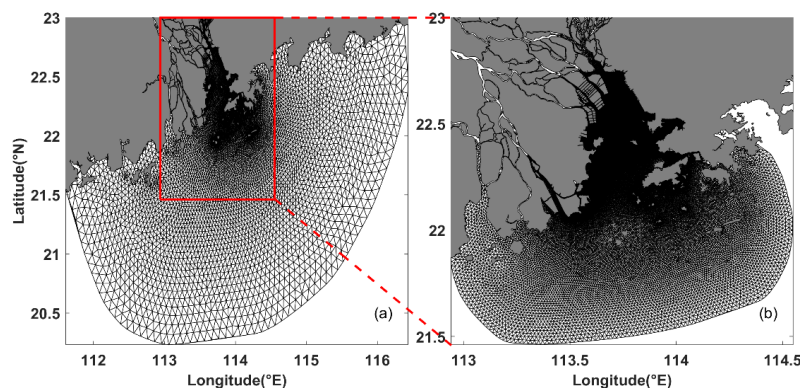


185 coupled component of eddy viscosity oscillation and the tidal-average velocity gradient (v_{Lk1u1}
186 and u_{Lk1u1}).

187 **2.2 Model configuration and experiments**

188 This study employs the Finite Volume Coastal Ocean Model (FVCOM; Chen et al., 2006)
189 to simulate the dynamic response of LRV to wind and stratification in the PRE. FVCOM is a
190 three-dimensional primitive equation Community Ocean Model (Chen et al., 2003) that utilizes
191 a finite-volume approach, accounting for a free-surface and employing prognostic techniques.
192 The model consists of unstructured triangular cells and employs terrain-following vertical
193 coordinates, allowing for a better fitness of the irregular coastline and complex topography
194 present in the estuary.

195 The model domain, covering the PRE and adjacent coastal regions, is depicted in Fig. 1,
196 spanning from 111.5°E to 116.5°E and 20°N to 23°N. The open boundary is situated in the
197 northern South China Sea. Unidirectional grid nesting is implemented to enhance solution
198 algorithms. The coarse grid consists of 8040 nodes and 15093 triangular elements. The spatial
199 resolution of the horizontal grids varies across the entire region, ranging from 1 to 10 km.
200 Specifically, a resolution of 1 km is employed within the PRE, 2.0–5.0 km off the Guangdong
201 coast, and 10 km near the open boundary (Fig. 1a). On the other hand, the fine grid comprises
202 45368 nodes and 87179 triangular elements. The spatial resolution of the fine grids within the
203 region also varies, ranging from 0.1 to 2.0 km. More specifically, a resolution of 0.1 km is
204 utilized within the PRE, 0.1–1.0 km off the Guangdong coast, and 2.0 km close to the open
205 boundary (Fig. 1b). In the vertical direction, the model employs fourteen uniformly assigned
206 sigma levels.



207

208

Figure 1. (a) Coarse mesh model, (b) fine mesh model.

209

210

211

212

213

214

215

216

217

218

219

220

221

222

223

224

The model incorporates eight major tidal constituents, namely M_2 , N_2 , S_2 , K_2 , K_1 , O_1 , P_1 , and Q_1 , as tidal driving forces at the open boundary. These constituents are obtained from the Oregon State University Tidal Prediction Software (OTPS). To initialize the model, salinity climatological data from the 1° World Ocean Atlas 2009 (WOA2009) dataset (<https://accession.nodc.noaa.gov/0094866>) is utilized. For wind forcing, monthly average wind data from the 0.25° CCMP dataset (<http://www.remss.com/measurements/ccmp>) is interpolated across the entire model domain. The lateral boundary incorporates monthly average river runoff data from eight river inlets, which are provided by the Water Conservancy Committee of the Pearl River under the Ministry of Water Resources. The topography data off the PRE is from the ETOPO2 dataset of NOAA, while the topography within the estuary is derived from electronic nautical chart data provided by the China Maritime Safety Administration.

The coarse grid model simulates a period from 1 January to 31 August 2017, and it reaches a quasi-steady state after one month. In this study, the outputs from the coarse grid model are utilized as the initial and boundary conditions for the fine grid model. The fine grid model, which begins in June, stabilizes after one month. The analysis focuses on the results from the fine grid model obtained on 24 July 2017 during spring tides and 2 August 2017 during neap



225 tides. A split-mode time stepping method is employed with 2-second external and 10-second
226 internal time steps for the coarse grid model, respectively. The fine grid model uses a 0.5-
227 second external time step, which is half of the time step used in the coarse grid model. The
228 bottom friction in the model is based on the quadratic bottom friction law, and the calculation
229 of the eddy viscosity coefficient employs the Mellor-Yamada 2.5 order turbulent closure model.

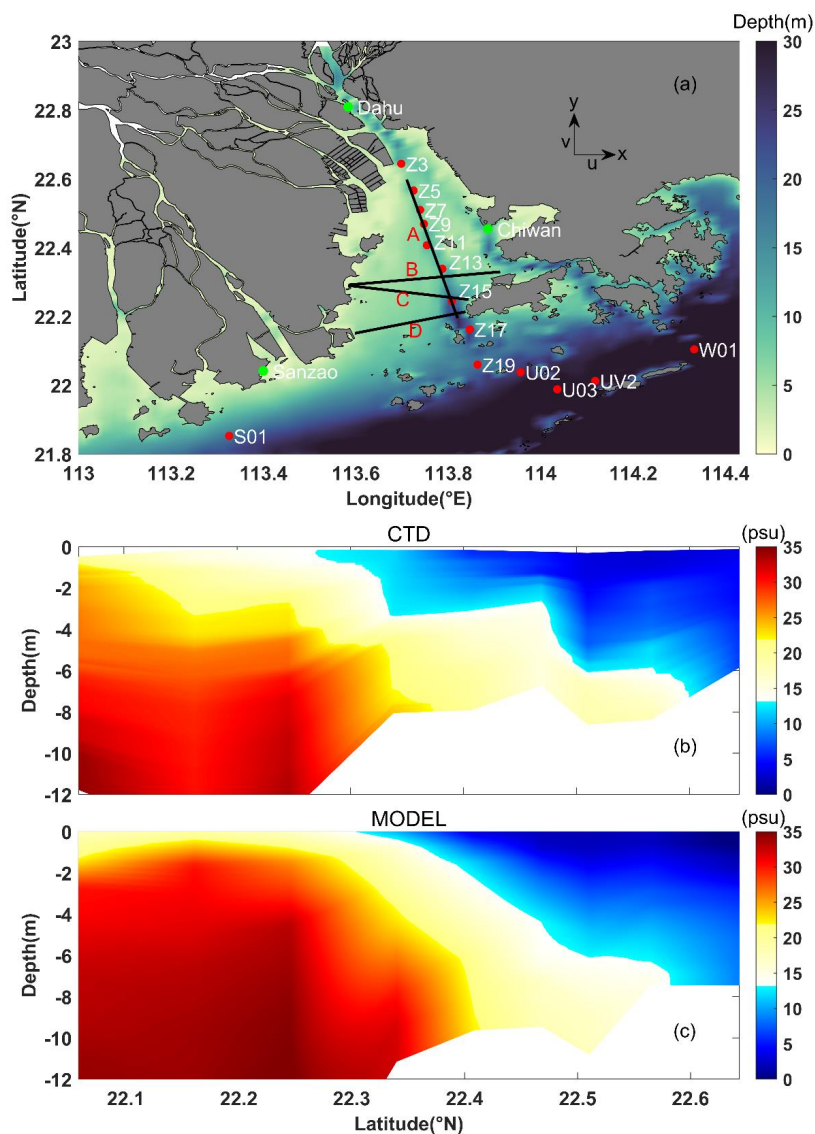
230 To investigate the effects of wind and stratification on the dynamics of LRV, Case 1
231 (reference case) includes wind forcing and periodic stratification. Case 2 examines the
232 influence of wind by removing wind forcing compared to Case 1. Case 3 explores the effects
233 of stratification by imposing a uniformly constant salinity and temperature without considering
234 river discharge compared to Case 2 (Table 1). The constant salinity and temperature, with
235 values of 28 °C and 32 psu, respectively, are derived by averaging WOA2009 data for July and
236 August across the whole domain.

Table 1. Numerical experiment scenarios

Experiments	Wind	Tide	Stratification
Case 1 (Reference case)	✓	✓	✓
Case 2	×	✓	✓
Case 3	×	✓	×

237 **2.3 Model verification**

238 The PRE is oriented in the north-south direction (Fig. 2). Accordingly, the positive x -axis,
239 u , and u_L direct eastward; the positive y -axis, v , and v_L direct northward; and the positive z -axis,
240 w , and w_L direct upward. In this context, u and v correspond to the cross-estuary and along-
241 estuary velocities, respectively, with u_L and v_L denoting the corresponding LRV. The paper
242 selects four sections, including three cross sections (Sections B–C) and one along-estuary
243 section (Section A), which roughly cover the PRE (black lines in Fig. 2a). Section C is chosen
244 to analyze the model results, and similar conclusions are drawn for the remaining three sections.



245

246 **Figure 2.** (a) Bathymetry of the model domain. Black lines mark sections for result analysis. Green dots
247 indicate tide gauge stations for elevation validation, and red dots indicate CTD positions for salinity
248 verification. (b) The along-estuary distributions of observed salinity interpolated from the CTD depth-
249 profiled data in section C, and (c) the salinity obtained from the numerical model.

250 Model verification involves comparing the model-derived elevation and salinity with the
251 corresponding observed values from the tide gauge and CTD stations, respectively (Fig. 3).



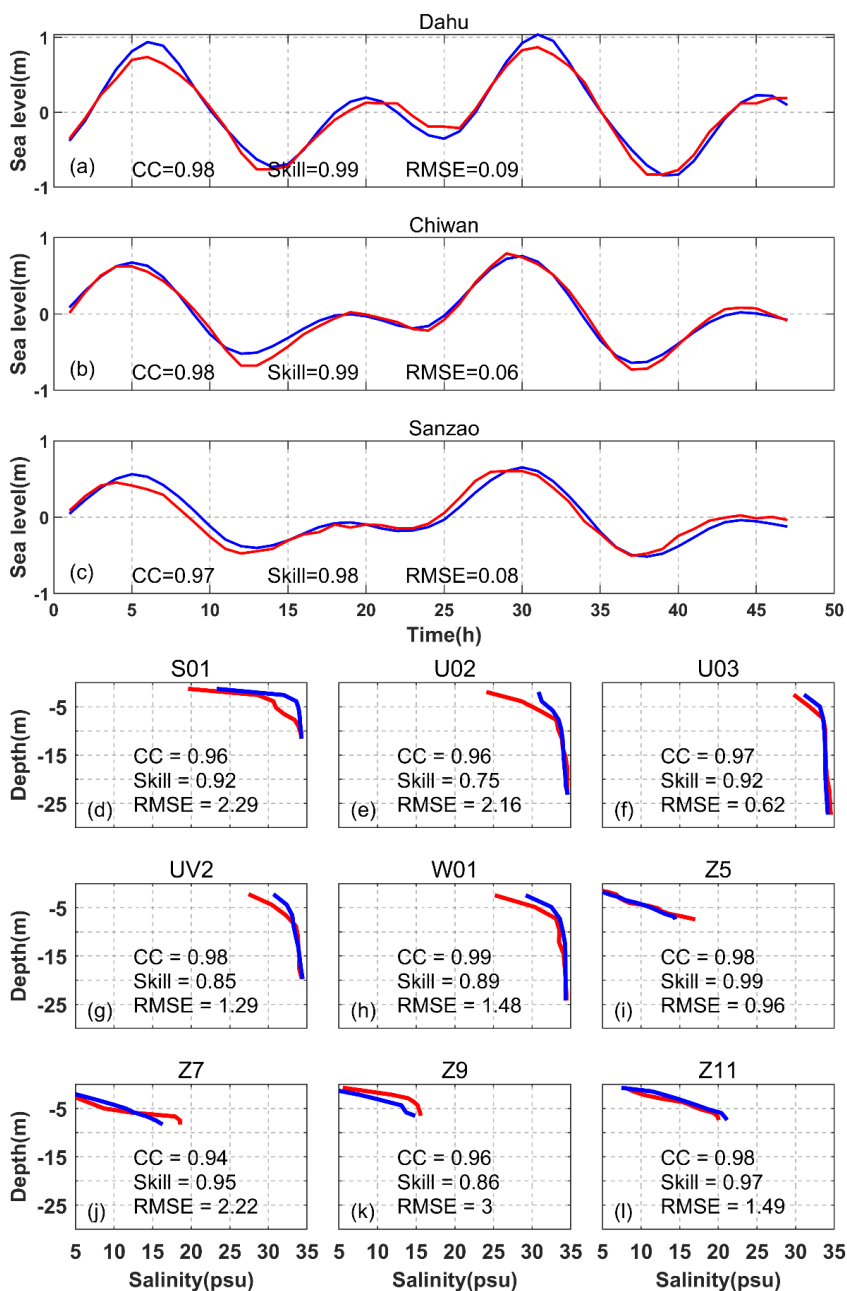
252 The observed sea surface elevation data are collected between 2 and 4 August 2017, and the
253 observed salinity data are acquired through CTD profiling from 4 to 6 August 2017. A good
254 agreement between the model and observed values highlights the effectiveness of the model
255 (Fig. 3). To further assess the model's performance, three statistical parameters are calculated:
256 the correlation coefficient (CC), Willmott Skill score (Willmott, 1981), and Root Mean Square
257 Error (RMSE). These parameters quantify the model's accuracy and skill:

$$CC = \frac{\sum_{i=1}^N (ob_i - \overline{ob})(mo_i - \overline{mo})}{\sqrt{\sum_{i=1}^N (ob_i - \overline{ob})^2 \sum_{i=1}^N (mo_i - \overline{mo})^2}}, \quad (4)$$

$$Skill = 1 - \frac{\sum_{i=1}^N (ob_i - mo_i)^2}{\sum_{i=1}^N (|mo_i - \overline{ob}| + |ob_i - \overline{ob}|)^2}, \quad (5)$$

$$\text{and } RMSE = \sqrt{\frac{1}{N} \sum_{i=1}^N (ob_i - mo_i)^2}, \quad (6)$$

258 where ob_i and mo_i are the observed data and model data, respectively, \overline{ob} and \overline{mo} are the
259 average value of the observed data and the model data, and N represents the number of
260 observations. The performance assessments of the modeled tidal elevation are presented in Figs.
261 3a–c. The model demonstrates a reasonable match with the observed tidal elevations,
262 exhibiting good performance with a skill score greater than 0.98, a correlation coefficient
263 exceeding 0.97, and a root mean square error less than 0.09 m. This indicates that the model
264 performs well in simulating tidal elevations. The assessments of the model's performance in
265 simulating salinity are depicted in Figs. 2b–c and Figs. 3d–l. The correlation coefficients for
266 salinity are higher than 0.94, with the majority of skill scores exceeding 0.85 and root mean
267 square errors less than 3 psu. The model exhibits well performance in simulating salinity.



268

269 **Figure 3.** Comparisons between the observed (red line) and modeled (blue line) elevation and salinity. The

270 three parameters including CC, Skill, and RMSE are calculated at each station.



271 **3. Results**

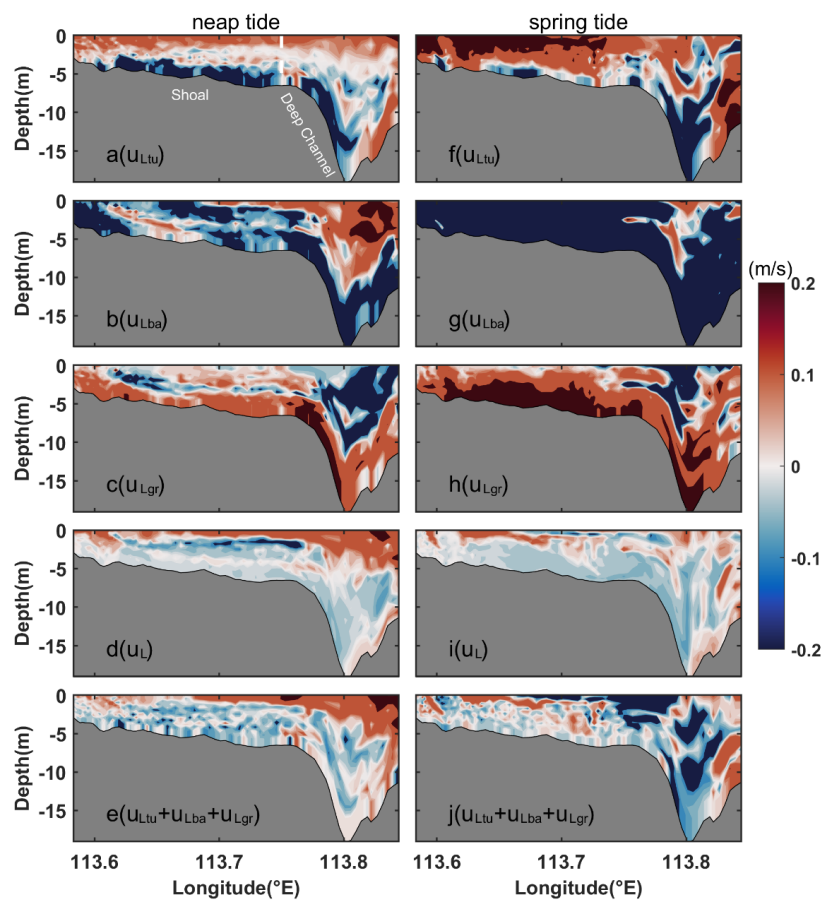
272 **3.1 Contributions of dominant components for LRV**

273 To quantify the contribution of each dynamic component of the LRV, the absolute values
274 of each component are averaged throughout Section C in this study, as follows:

$$M(\cdot) = \frac{1}{B} \int abs(\cdot) dB, \quad (7)$$

275 where *abs* are the absolute value function, the symbol \cdot can be replaced by each dynamic
276 component of the LRV, and *B* represents the area of the cross-section.

277 Figure 4 illustrates the decomposition of cross-estuary LRV into dominant contributions
278 for the reference case. During neap tides, the eddy viscosity component (u_{Ltu}) exhibits a two-
279 layer structure with eastward flow in the upper layer and westward flow in the lower layer (Fig.
280 4a). The barotropic pressure gradient component (u_{Lba}) generally flows westward in most areas
281 of the shoal, while it displays an eastward flow in the upper layer and a westward flow in the
282 lower layer of the deep channel (Fig. 4b). Conversely, the contribution from the baroclinic
283 pressure gradient (u_{Lgr}) opposes u_{Lba} (Fig. 4c). During spring tides, the structure of the three
284 components, namely u_{Ltu} , u_{Lba} , and u_{Lgr} , remains analogous to that during neap tides throughout
285 the cross section (Figs. 4f–h). During both spring and neap tides, the three striking components
286 (u_{Ltu} , u_{Lgr} and u_{Lba}) are aggregated (Figs. 4e and j) and compared to the total LRV obtained
287 directly from the model based on the Lagrangian particle tracking algorithms (Figs. 4d and i).
288 It is observed that u_L primarily arises from an imbalance between u_{Ltu} , u_{Lgr} , and u_{Lba} . The
289 eastward exchange circulation is predominantly attributed to u_{Ltu} in the upper layer of the shoal,
290 while the westward flow in the lower layer of the shoal is primarily driven by u_{Ltu} and u_{Lba} . In
291 the upper layer of the deep channel, the eastward flow is determined by the interplay of u_{Lba}
292 and u_{Ltu} , which also induces the westward flow in the lower layer of the channel. Notably, u_{Lgr}
293 predominantly counteracts u_{Lba} .



294

295 **Figure 4.** The structure of each dominant component of u_L in Section C for Case 1. (a) the eddy viscosity
 296 component, (b) the barotropic component, (c) the baroclinic component, (d) the total LRV directly obtained
 297 by the model, and (e) the sum of the eddy viscosity component, barotropic component, and baroclinic
 298 component during neap tides. The counterparts during spring tides are shown in the right column. Red
 299 shading represents eastward flow, and blue shading represents westward flow.

300 The intensities of the exchange flows are quantified in Table 2 for the reference case.
 301 During spring tides, the magnitude of u_{Ltu} is approximately 2 times higher than that during neap
 302 tides, the magnitude of u_{Lgr} nearly doubles compared to that during neap tides, and the
 303 magnitude of u_{Lba} is roughly 4 times as large as that during neap tides. Among the dominant
 304 components of u_L , u_{Lba} exhibits the most pronounced contributions, being 1–2 times as strong



305 as u_{Lu} and u_{Lgr} .

306

Table 2. The magnitude of each component of u_L and v_L

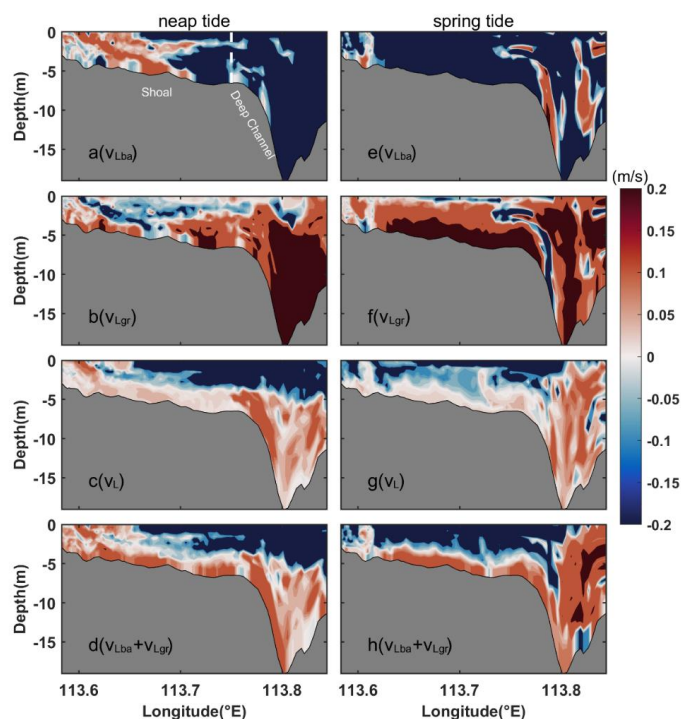
	Case 1 (neap)	Case 1 (spring)	Case 2 (neap)	Case 2 (spring)	Case 3 (neap)	Case 3 (spring)
$M(u_{Lba})$	0.12	0.43	0.15	0.42	0.04	0.17
$M(u_{Lgr})$	0.10	0.23	0.11	0.23	—	—
$M(u_{Lu})$	0.09	0.23	0.07	0.20	0.03	0.16
$M(u_{Lac})$	0.09	0.13	0.09	0.14	0.02	0.09
$M(u_{Ladh})$	0.13	0.19	0.13	0.18	0.02	0.09
$M(u_{Ladv})$	0.08	0.11	0.09	0.11	0.0041	0.10
$M(u_{Lho})$	0.01	0.01	0.01	0.01	0.0007	0.0049
$M(v_{Lba})$	0.17	0.25	0.30	0.36	0.02	0.06
$M(v_{Lgr})$	0.15	0.22	0.25	0.28	—	—
$M(v_{Lu})$	0.06	0.09	0.04	0.10	0.02	0.06
$M(v_{Lac})$	0.10	0.13	0.10	0.13	0.03	0.08
$M(v_{Ladh})$	0.12	0.14	0.12	0.14	0.03	0.08
$M(v_{Ladv})$	0.04	0.05	0.05	0.05	0.0006	0.0054
$M(v_{Lho})$	0.01	0.01	0.01	0.01	0.0004	0.0023

307

308 The decomposition of along-estuary LRV into dominant contributions is depicted in Fig.
 309 5 for the reference case. During neap tides, the barotropic pressure gradient component (v_{Lba})
 310 contributes to an up-estuary flow in most areas of the shoal and a down-estuary flow in the
 311 deep channel (Fig. 5a); the baroclinic pressure gradient component (v_{Lgr}) exhibits a two-layer
 312 circulation with seaward flow in the upper layer and landward flow in the lower layer of the
 313 shoal along with inflow in most areas of the deep channel (Fig. 5b). It shows the opposite
 314 pattern to v_{Lba} . During spring tides, there is a down-estuary flow of v_{Lba} in the shoal, which is
 315 contrary to the flow pattern during neap tides (Fig. 5e). Additionally, the outflow area of v_{Lgr}



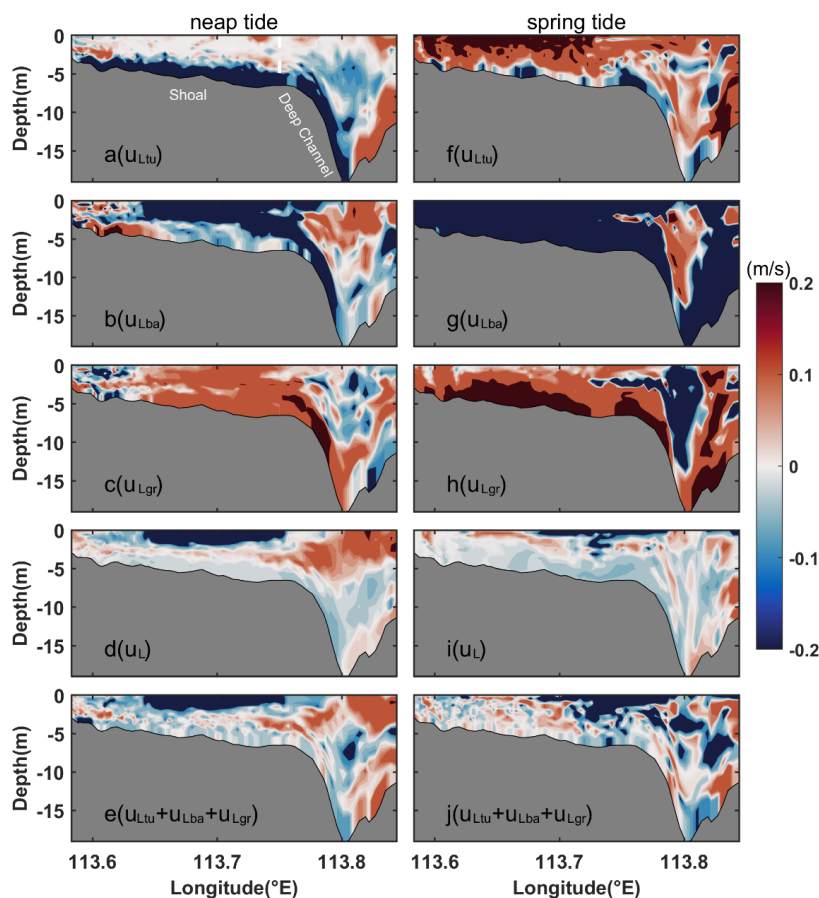
316 in the upper layer of the shoal is smaller during spring tides than during neap tides (Fig. 5f).
317 Both during spring and neap tides, the sum of v_{Lba} and v_{Lgr} (Figs. 5d and h) closely resembles
318 the total along-estuary LRV (v_L) (Figs. 5c and g). Therefore, the dominant components of v_L
319 are v_{Lba} and v_{Lgr} . Since these components must balance across the estuary, the outflow in the
320 upper layer is mainly determined by v_{Lba} , while the inflow in the lower layer is induced by v_{Lgr} .
321 During spring tides, the magnitudes of v_{Lba} and v_{Lgr} are 1.4 times as large as those during neap
322 tides (Table 2). The contributions from gravitational circulation and barotropic pressure
323 gradient component to total LRV are of the same magnitude.



324
325 **Figure 5.** The structure of each dominant component of v_L in Section C for Case 1. (a) barotropic pressure
326 gradient component, (b) baroclinic pressure gradient component, (c) the total LRV obtained directly by the
327 model, and (d) the sum of barotropic and baroclinic pressure gradient components during neap tides. The
328 counterparts during spring tides are shown in the right column. Red shading represents inflow to the estuary,
329 and blue shading represents outflow to the sea.



330 Neglecting the influence of wind, the cross-estuary dominant components are displayed
331 in Fig. 6 for Case 2. The eddy viscosity component (u_{Ltu}) exhibits a similar pattern to the
332 reference case both during neap and spring tides (Figs. 6a and f). However, during neap tides,
333 the magnitude of the eastward flow of u_{Ltu} in the upper 2 m is approximately one order of
334 magnitude smaller than that in Case 1 (Fig. 6a vs. Fig. 4a), although the absolute value of u_{Ltu}
335 averaged in Section C for Case 2 is slightly different compared to that in Case 1 (Table 2). This
336 suggests that wind primarily affects the upper exchange circulation by influencing the mixing
337 of the upper water column. During spring tides, u_{Ltu} shows small differences in magnitude
338 between Case 1 and Case 2 (Fig. 6f vs. Fig. 4f), indicating that wind sheds a slight influence
339 on exchange flow during spring tides. During both spring and neap tides, the structures and
340 magnitudes of the barotropic pressure gradient component (u_{Lba}) and the baroclinic pressure
341 gradient component (u_{Lgr}) are similar to that in Case 1. When wind effects are not considered,
342 the structure of the cross-estuary LRV (u_L) (Figs. 6d and i) is still determined by the combined
343 contributions of u_{Lba} , u_{Lgr} , and u_{Ltu} (Figs. 6e and j). However, the eastward flow determined by
344 u_{Ltu} in the upper layer of the shoal in Case 1 transforms into a westward flow primarily driven
345 by u_{Lba} in Case 2.



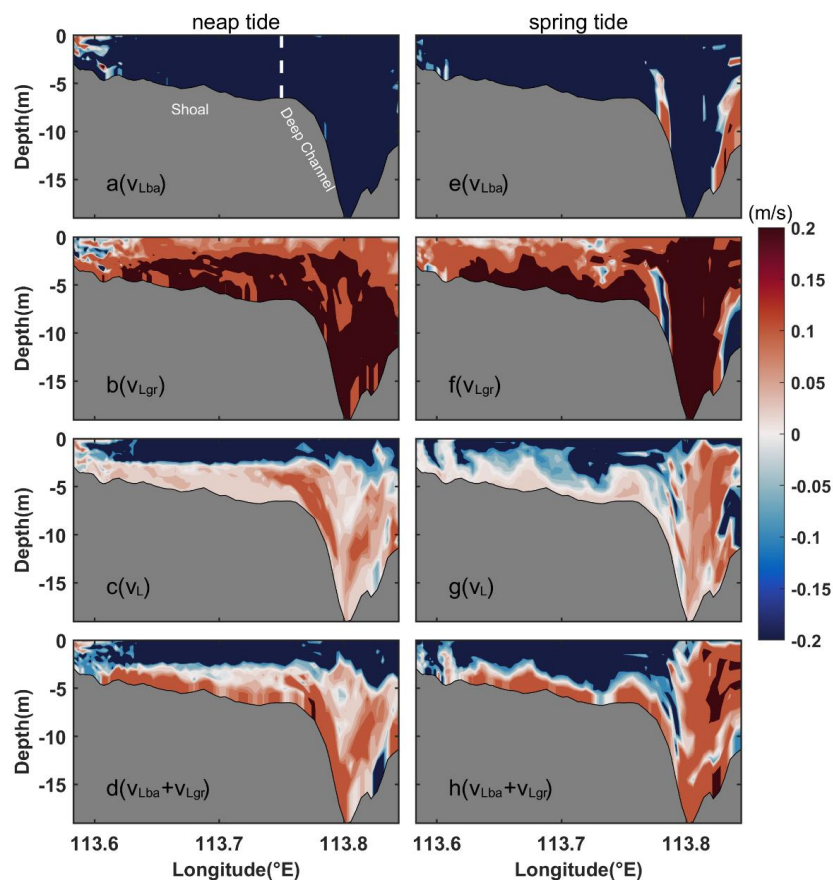
346

347 **Figure 6.** Same as Figure 4, but for Case 2 without wind forcing.

348 The along-estuary dominant components in Case 2 are shown in Fig. 7. The v_{Lba} changes
 349 from inflow in Case 1 to outflow in the shoal during neap tides (Fig. 7a). Similarly, v_{Lgr} shifts
 350 from outflow in Case 1 to inflow in the upper layer of the shoal during neap tides in Case 2
 351 (Fig. 7b). This suggests that wind plays a crucial role in the components of LRV in the upper
 352 water column of the shoal. During spring tides, v_{Lba} and v_{Lgr} maintain the same structure as
 353 observed in Case 1 (Figs. 7e and f), indicating that wind is unimportant during spring tides.
 354 The structure of the along-estuary LRV (v_L) (Figs. 7c and g) is primarily determined by the
 355 combined contributions of v_{Lba} and v_{Lgr} (Figs. 7d and h), analogous to that in Case 1. But in the



356 absence of wind, the magnitudes of v_{Lba} and v_{Lgr} are larger than those in Case 1, indicating that
 357 southwesterly wind suppresses gravitational circulation. The relative contributions of v_{Lba} and
 358 v_{Lgr} to v_L are approximately equal (Table 2).



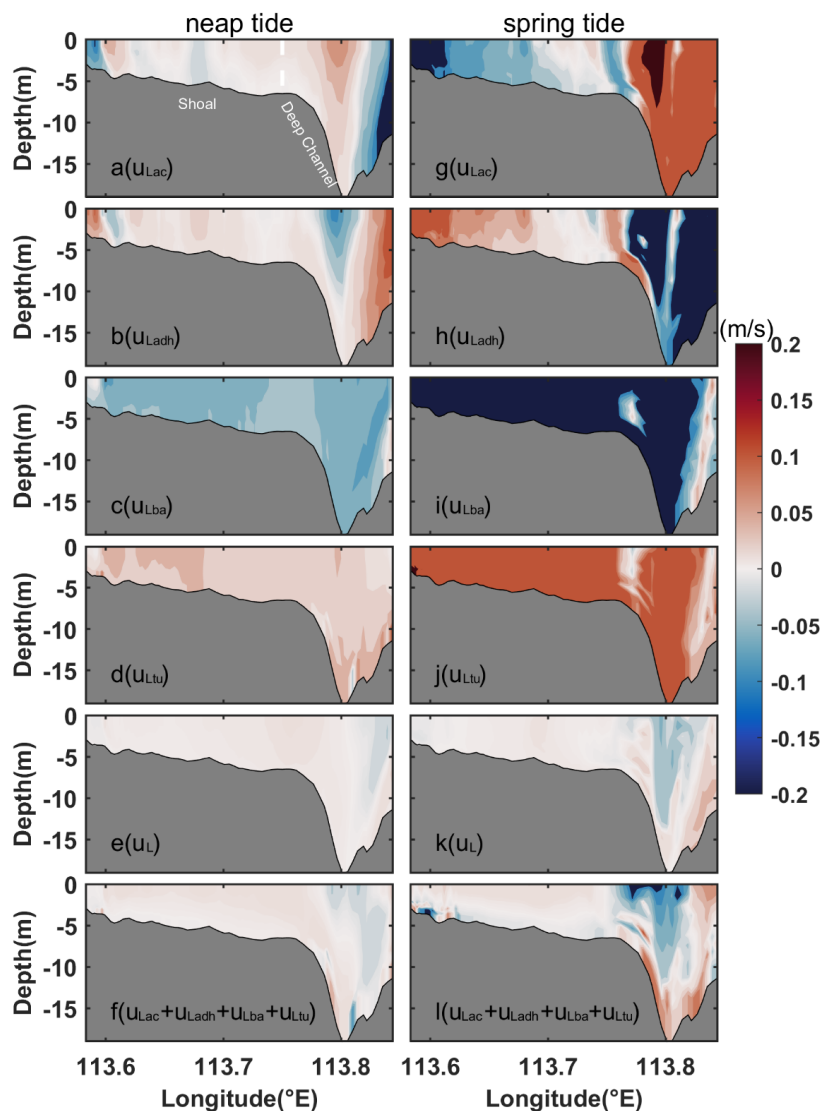
359

360 **Figure 7.** Same as Figure 5, but for Case 2 without wind forcing.

361 The stratification and wind forcing are ignored in Case 3. The dominant components of
 362 the cross-estuary LRV in Section C are shown in Fig. 8. During neap tides, the local
 363 acceleration component (u_{Lac}) predominantly exhibits eastward flow in most areas, with minor
 364 regions showing westward flow in the shoal and deep channel (Fig. 8a). Conversely, during
 365 spring tides, a prevailing westward flow characterizes the majority of the shoal regions, while



366 an eastward flow prevails in the deep channel (Fig. 8g). These results highlight the significant
367 impact of tides on the structure of u_{Lac} in a homogeneous water column. Comparing the results
368 with those of Case 2, u_{Lac} undergoes a transition from vertically sheared flow in Case 2 to
369 horizontally sheared flow in Case 3, indicating that stratification plays a notable role in shaping
370 the structure of u_{Lac} . The horizontal nonlinear advective component (u_{Ladh}) exhibits a flow
371 pattern that is the reverse of u_{Lac} (Figs. 8b and h). The barotropic pressure gradient component
372 (u_{Lba}) primarily shows unidirectional westward flow throughout the cross section (Figs. 8c and
373 i). The pattern of u_{Lba} in the shoal and most of the lower layer of the deep channel is consistent
374 with that observed in Case 2. However, in the upper layer of the deep channel, u_{Lba} transforms
375 eastward flow in Case 2 into westward flow in Case 3. The eddy viscosity component (u_{Ltv})
376 induces a flow opposite to that of u_{Lba} (Figs. 8d and j), which differs from the vertically sheared
377 flow observed in Case 2.



378

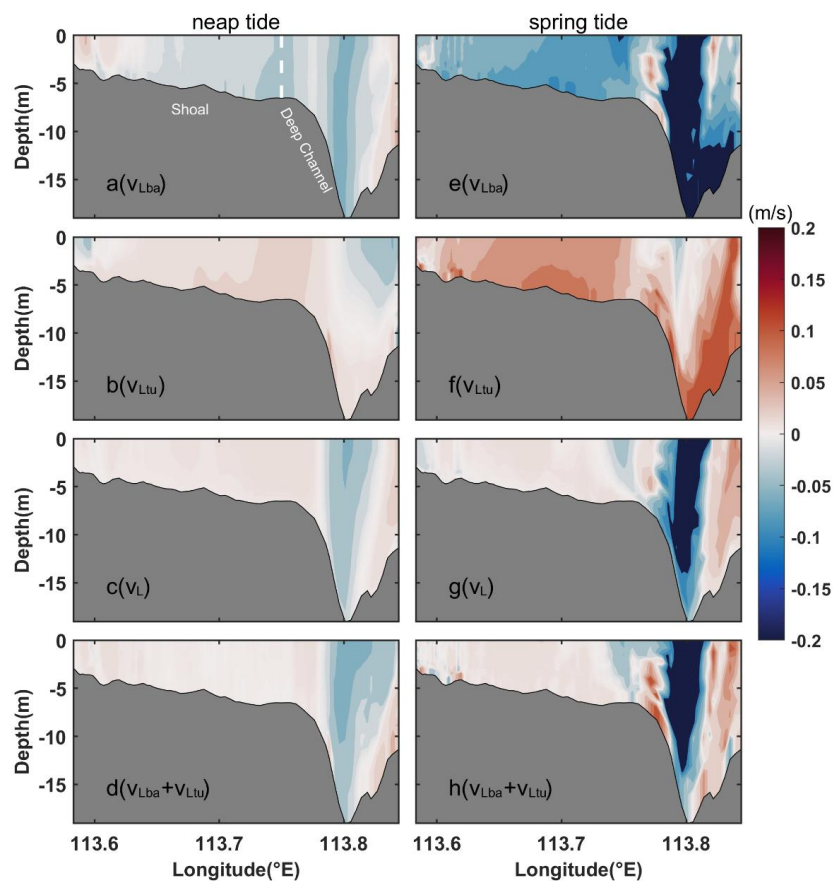
379 **Figure 8.** The structure of each dominant component of u_L in Section C for Case 3. (a) local acceleration
 380 component, (b) horizontal nonlinear advection component, (c) barotropic pressure gradient component, (d)
 381 eddy viscosity component, (e) the total LRV obtained directly by the model, and (f) sum of local acceleration
 382 component, horizontal nonlinear advection component, barotropic pressure gradient component, and eddy
 383 viscosity component during neap tides. The counterparts during spring tides are shown in the right column.
 384 Red shading represents eastward flow and blue shading represents westward flow.



385 The structure of the cross-estuary LRV (u_L) (Figs. 8e and k) closely resembles the structure
386 of the sum of the four components: u_{Lac} , u_{Ladh} , u_{Lba} , and u_{Ltu} in Case 3 (Figs. 8f and l). This
387 indicates that the overall structure of u_L (Figs. 8e and k) is primarily determined by the
388 combined effects of these four components. Among them, the eastward flow in the shoal and
389 the lower layer of the deep channel is mainly determined by u_{Ltu} (Figs. 8d and j), with u_{Lac}
390 playing a secondary role (Figs. 8a and g). On the other hand, the westward flow in the upper
391 layer of the deep channel is primarily influenced by u_{Lba} (Figs. 8c and i), with u_{Ladh} contributing
392 as a secondary component (Figs. 8b and h).

393 The magnitudes of u_{Lac} , u_{Ladh} , and u_{Lba} during spring tides are approximately four times
394 as large as those during neap tides in Case 3 (Table 2). The magnitude of u_{Ltu} during spring
395 tides is 4.8-fold compared to neap tides. The relative contributions of u_{Lba} and u_{Ltu} to u_L are
396 roughly equal, and u_{Lac} and u_{Ladh} have similar contributions. Moreover, the contribution of u_{Lba}
397 is approximately 1–2 times as large as that of u_{Lac} .

398 Both during spring and neap tides, the along-estuary barotropic pressure gradient
399 component (v_{Lba}) exhibits outflow in most areas in Case 3 (Figs. 9a and 9e), which is similar
400 to Case 2, indicating that stratification has minimal effects on the structure of v_{Lba} . The eddy
401 viscosity component (v_{Ltu}) shows a nearly opposite pattern compared to v_{Lba} (Figs. 9b and f).
402 Compared to Case 2, the pattern of v_{Ltu} exhibits significant changes at the bottom of the shoal
403 and in the deep channel. The imbalance between the two components, v_{Lba} and v_{Ltu} (Figs. 9d
404 and h), determines the along-estuary circulation (v_L) (Figs. 9c and g). The inflow in the shoal
405 is primarily driven by v_{Ltu} , while the outflow in the deep channel is dominated by v_{Lba} . During
406 spring tides, the magnitudes of v_{Lba} and v_{Ltu} are about 4-fold that during neap tides (Table 2).
407 During neap and spring tides, the relative contributions of v_{Lba} and v_{Ltu} to v_L are equal.



408

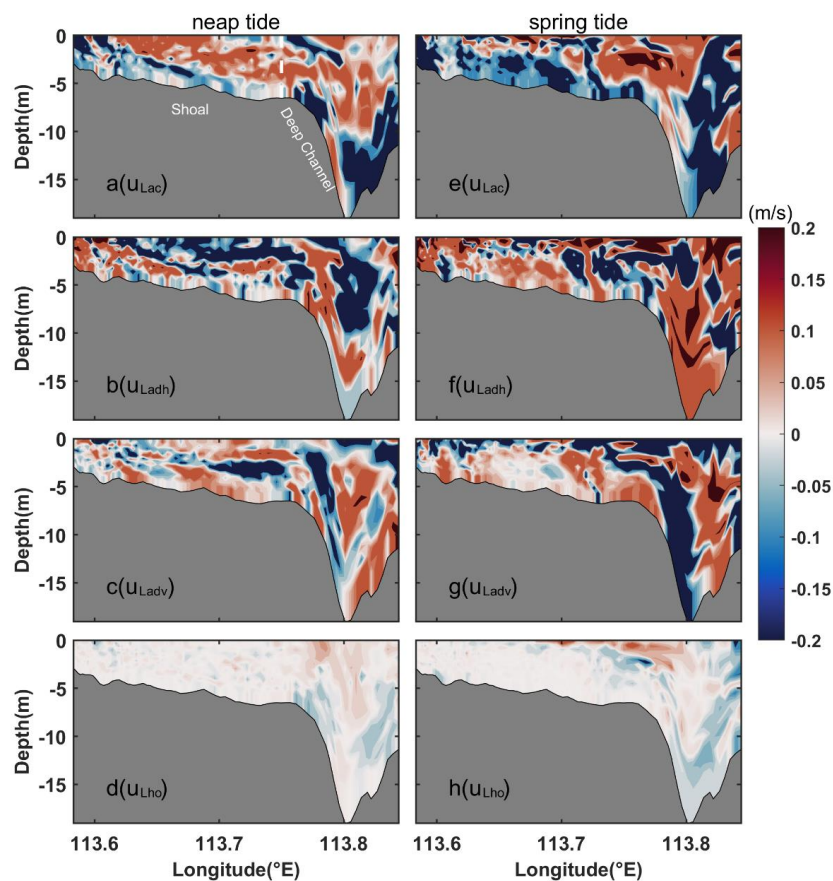
409 **Figure 9.** The structure of each dominant component of v_L in Section C for Case 3. (a) the barotropic pressure
 410 gradient component, (b) the eddy viscosity component, (c) the total LRV obtained directly by the model, and
 411 (d) the sum of barotropic pressure gradient component and eddy viscosity component. The counterparts
 412 during spring tides are shown in the right column. Red shading represents inflow to the estuary, and blue
 413 shading represents outflow to the sea.

414 3.2 Contributions of Non-dominant Components for LRV

415 The analysis of the contributions from non-dominant components to LRV for Case 1 is
 416 depicted in Fig. 10. During neap tides, the local acceleration (u_{Lac}) induces eastward flow in
 417 the majority of the upper layer and westward flow in the lower layer (Fig. 10a). Conversely,



418 the horizontal nonlinear advection component (u_{Ladh}) exhibits an opposite pattern to u_{Lac} across
419 most regions (Fig. 10b). Meanwhile, the vertical nonlinear advective component (u_{Ladv}) serves
420 as a sandwiched structure, characterized by vertically staggered eastward and westward flow
421 (Fig. 10c). The combined configuration of u_{Lac} and u_{Ladh} contrasts with that of u_{Ladv} , yielding a
422 relatively small and negative contribution from the sum of these three components to u_L .
423 Consequently, the three components are denoted as non-dominant components. The
424 magnitudes of the non-dominant components of u_L during spring tides are slightly larger than
425 those during neap tides. The general patterns of these three components during spring tides
426 closely resemble those during neap tides (Figs. 10e–g). Moreover, both during spring and neap
427 tides, the horizontal diffusion component (u_{Lho}) is smaller compared to the other components
428 (Figs. 10d and h), and its contribution is negligible.



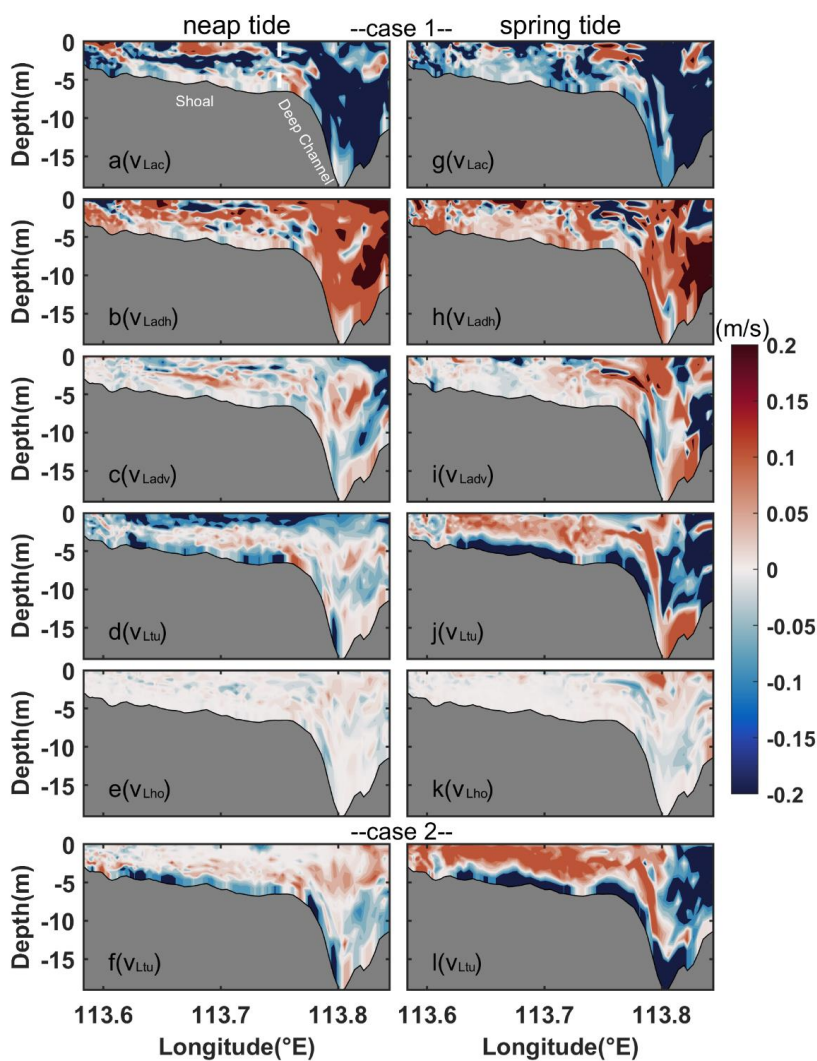
429

430 **Figure 10.** Vertical section of each non-dominant component of u_L in Section C for Case 1. (a) local
 431 acceleration component, (b) horizontal nonlinear advection component, (c) vertical nonlinear advection
 432 component, and (d) horizontal diffusion component during neap tides. The counterparts during spring tides
 433 are shown in the right column. Red shading represents eastward flow and blue shading represents westward
 434 flow.

435 During neap tides, the local acceleration component (v_{Lac}) exhibits a three-layer structure
 436 in the shoal, with inflow in the upper and lower layer and outflow in the middle layer. In the
 437 deep channel, unidirectional outflow prevails (Fig. 11a). The pattern of the horizontal nonlinear
 438 advective component (v_{Ladh}) is nearly the reverse of v_{Lac} (Fig. 11b). The vertical nonlinear term
 439 (v_{Ladv}) results in down-estuary flow in the upper and lower layer while up-estuary flow



440 dominates in the middle layers (Fig. 11c). The combination of three components contributes to
441 total LRV less and negatively. Additionally, the eddy viscosity-induced flow (v_{Ltu}) during neap
442 tides exhibits a vertical shear structure, with outflow in the upper and lower layer and inflow
443 in the middle layer (Fig. 11d). During spring tides, the overall structures for each non-dominant
444 component resemble those during neap tides; however, the magnitudes during spring tides
445 exceed those recorded during neap tides (Figs. 11g–j). For both spring and neap tides, the
446 contributions of the horizontal diffusion components (v_{Lho}) are negligible (Figs. 11e and k;
447 Table 2). Moreover, the contribution of v_{Ltu} is relatively smaller compared to their respective
448 dominant components (Table 2). In the absence of wind effects, the structure and contribution
449 of each non-dominant component of the cross-estuary LRV (u_L) in Case 2 closely resemble
450 those observed in Case 1 during both spring and neap tides (not shown), with the exception of
451 the noticeably reduced along-estuary eddy viscosity component (v_{Ltu}) in the upper layer in Case
452 2 during neap tides (Fig. 11f) and slightly intensified v_{Ltu} during spring tides (Fig. 11i). These
453 indicate that wind has a weak influence on the non-dominant components of cross-estuary
454 circulation. However, wind significantly affects the non-dominant component v_{Ltu} of the along-
455 estuary circulation in the upper layer.
456



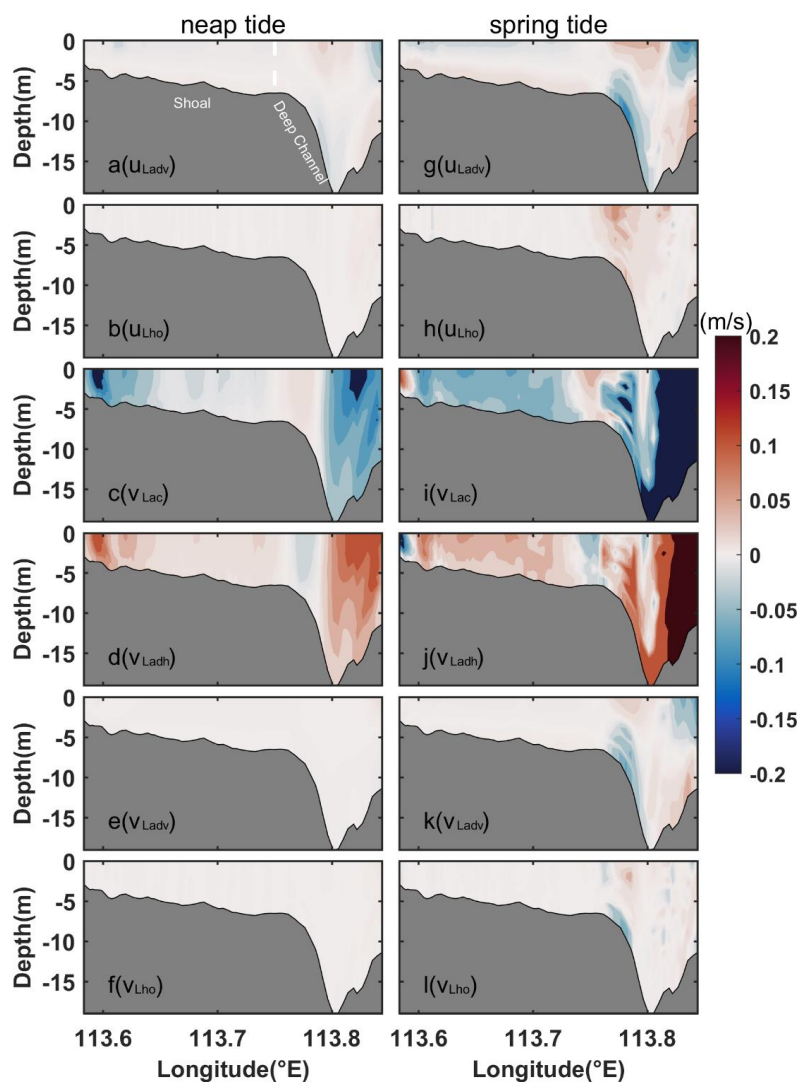
457

458 **Figure 11.** Vertical section of each non-dominant component of v_L in Section C for Case 1 (a–e; g–k) and
 459 Case 2 (f and l). (a) local acceleration component, (b) horizontal nonlinear advection component, (c) vertical
 460 nonlinear advection component, (d) eddy viscosity component, and (e) horizontal diffusion component
 461 during neap tides for Case 1. (f) eddy viscosity component during neap tides for Case 2. The counterparts
 462 during spring tides are shown in the right column. Red shading represents inflow, and blue shading represents
 463 outflow.

464 Neglecting wind forcing and stratification, the magnitudes of the vertical nonlinear



465 advection component (u_{Ladv}) and horizontal diffusion component (u_{Lho}) are relatively low
466 during both spring and neap tides. Compared to Case 2, the magnitude of u_{Lho} (Figs. 12b and
467 h) in Case 3 is reduced by half during spring tides and by a factor of 14 during neap tides, while
468 the magnitude of u_{Ladv} (Figs. 12a and g) in Case 3 experiences a tenfold reduction during spring
469 tides and a twentyfold reduction during neap tides (Table 2). For both neap and spring tides,
470 v_{Lac} shifts from inflow in Case 2 to outflow in Case 3 in some areas of the shoal (Figs. 12c and
471 i). The horizontal nonlinear advection component (v_{Ladh}) in Case 3 exhibits a pattern opposite
472 to that of v_{Lac} (Figs. 12d and j). Their combined contributions of these two components to total
473 LRV can be disregarded. The contributions from the vertical nonlinear advection component
474 (v_{Ladv}) and horizontal diffusion component (v_{Lho}) during spring and neap tides remain relatively
475 low in Case 3 (Figs. 12e, k, f, and l). The magnitude of v_{Lho} in Case 3 is fivefold smaller during
476 spring tides and 25 times smaller during neap tides than those in Case 2, while the magnitude
477 of v_{Ladv} in Case 3 experiences an approximately tenfold reduction during spring tides and an
478 eightyfold reduction during neap tides compared to Case 2 (Table 2).



479

480 **Figure 12.** The vertical distribution of each non-dominant component of u_L and v_L in Section C for Case 3.

481 (a) cross-estuary vertical nonlinear advection component, (b) cross-estuary horizontal diffusion component,

482 (c) along-estuary local acceleration component, (d) along-estuary horizontal advection component, (e)

483 along-estuary vertical advection component, and (f) along-estuary horizontal diffusion during neap tides.

484 Red shading in (a) and (b) indicates eastward flow and blue shading indicates westward flow. Red shading

485 area in (c)–(f) represents inflow, and the blue shading area represents outflow. The counterparts during spring

486 tides are shown in the right column.



487 **3.3 Contributions of dominant components for the eddy viscosity component**

488 Through an analysis of dominant mechanisms influencing LRV under various dynamic
489 factors, the results reveal that the cross-estuary eddy viscosity component significantly shapes
490 the structure of cross-estuary LRV due to the prevailing southwesterly wind during the summer
491 in the PRE. However, the along-estuary eddy viscosity component is not the predominant
492 contributor to along-estuary LRV under stratified circumstances. In the case of destratification,
493 both the along-estuary and cross-estuary eddy viscosity components play roles in shaping the
494 total LRV. A comprehensive exploration of the dominant mechanisms of the eddy viscosity
495 component entails further decompositions of both the along-estuary and cross-estuary eddy
496 viscosity components into four subgroups. This analysis provides general conclusions and
497 implications for future studies. These subgroups encompass the coupled component of tidal-
498 averaged eddy viscosity and velocity gradient oscillation, the tidal straining component, the
499 turbulent mean component, and the coupled component of tidal-averaged velocity gradient and
500 eddy viscosity oscillation.

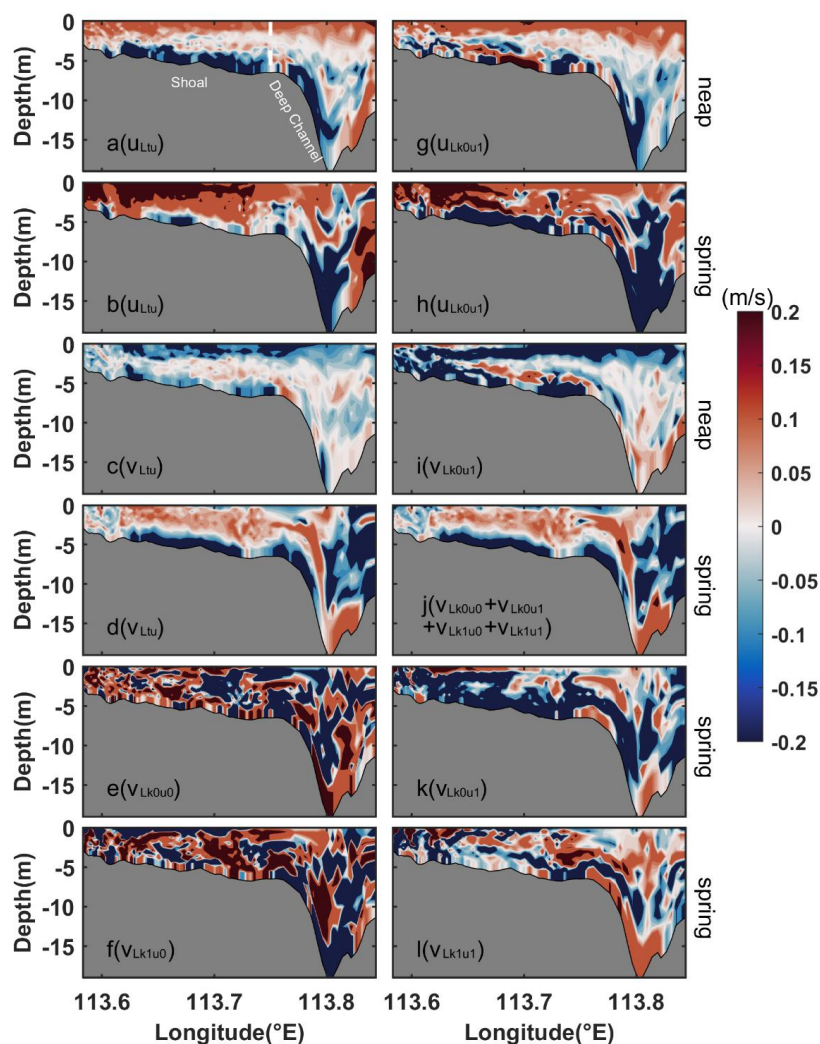
501 During neap tides, the cross-estuary turbulent mean component (u_{Lk0u1}) for Case 1 displays
502 eastward flows in the upper layer and westward flows in the lower layer (Fig. 13g). During
503 spring tides, u_{Lk0u1} closely resembles the pattern observed during neap tides (Fig. 13h). The
504 structure of u_{Lk0u1} during neap and spring tides is identical to that of the eddy viscosity (u_{Ltu})
505 (Figs. 13a and b). Therefore, u_{Ltu} is predominantly influenced by u_{Lk0u1} . During neap tides, the
506 along-estuary turbulent mean component (v_{Lk0u1}) for Case 1 exhibits a three-layer structure in
507 the shoal, with outflow occurring in the surface and bottom layers, and inflow in the middle
508 layer (Fig. 13i). In the deep channel, there is a two-layer flow pattern with outflow in the upper
509 layer and inflow in the lower layer. This structure aligns with that of the eddy viscosity
510 component (v_{Ltu}) (Fig. 13c). Hence, during neap tides, v_{Ltu} is primarily influenced by v_{Lk0u1} .
511 During spring tides, the structure of v_{Ltu} for Case 1 (Fig. 13d) is contributed by the combined



512 effect of the four components: v_{Lk0u0} , v_{Lk0u1} , v_{Lk1u0} , and v_{Lk1u1} (Fig. 13j), which differs from the
513 structure observed during neap tides. The inflow occurring in the upper layer of the shoal is
514 primarily determined by v_{Lk0u0} and v_{Lk1u0} (Figs. 13e and f), and the outflow in the lower layer
515 of the shoal is mainly influenced by v_{Lk0u1} (Fig. 13k). The structure in the deep channel is
516 primarily determined by v_{Lk0u1} .

517

518



519

520 **Figure 13.** Vertical section of cross-estuary (u_{Ltu}) and along-estuary (v_{Ltu}) eddy viscosity and the
 521 corresponding dominant components in Section C for Case 1. The u_{Ltu} during (a) neap tides and (b) spring
 522 tides, and (g) and (h) the corresponding dominant components of turbulent mean component (u_{Lk0u1}). The
 523 v_{Ltu} during (c) neap tides and (d) during spring tides, (i) the corresponding dominant components of turbulent
 524 mean component (v_{Lk0u1}), and (j) the sum of four dominant components (e, f, k, and g). The red shading
 525 represents eastward flow, and the blue shading represents westward flow for the cross-estuary components.
 526 For the along-estuary components, the red shading indicates inflow and the blue shading indicates outflow.



527 During neap tides, the cross-estuary turbulent mean component (u_{Lk0u1}) for Case 2 exhibits
528 eastward flow in the upper layer and westward flow in the lower layer (Fig. 14b). This pattern
529 aligns with Case 1. However, the magnitude of the eastward flow in the upper layer of u_{Lk0u1}
530 during neap tides is one order of magnitude smaller than that observed in Case 1. During spring
531 tides, the structure and magnitude of u_{Lk0u1} for Case 2 are similar to those of Case 1 (Fig. 14j),
532 suggesting a weak influence of wind on u_{Lk0u1} . Similar to Case 1, both during neap and spring
533 tides, the cross-estuary eddy viscosity component (u_{Ltu}) (Figs. 14a and i) is predominantly
534 determined by u_{Lk0u1} (Figs. 14b and j). During neap tides, the along-estuary turbulent mean
535 component (v_{Lk0u1}) for Case 2 exhibits inflow in the upper layer and outflow in the lower layer
536 (Fig. 14d). The structure of v_{Lk0u1} in the lower layer is consistent with that in Case 1, while the
537 structure in the upper layer is opposite to that of Case 1. Without the influence of wind, the
538 structure of v_{Lk0u1} in the upper layer shifts from outflow in Case 1 to inflow. During spring tides,
539 the area and magnitude of inflow in the upper layer of v_{Lk0u1} for Case 2 are larger than those
540 during neap tides (Fig. 14l). Both during neap and spring tides, the along-estuary eddy viscosity
541 component (v_{Ltu}) (Figs. 14c and k) exhibits the same structure as v_{Lk0u1} (Figs. 14d and l). Hence,
542 v_{Ltu} is predominantly influenced by the turbulent mean component (v_{Lk0u1}).

543 Without consideration of stratification, the cross-estuary tidal straining component (u_{Lk1u0})
544 for Case 3 exhibits eastward flow (Fig. 14f) in the shoal during neap tides. The u_{Lk1u0} undergoes
545 a transition from westward flow in Case 2 to eastward flow in the lower layer. During spring
546 tides, the u_{Lk1u0} for Case 3 maintains the same pattern as observed during neap tides, and its
547 magnitude is greater than that during neap tides (Fig. 14n). During neap tides, the along-estuary
548 tidal straining component (v_{Lk1u0}) for Case 3 exhibits inflow in most areas of the shoal, and
549 shows a two-layer structure in the deep channel with outflow in the upper layer, and inflow in
550 the lower layer (Fig. 14h), which is analogous to the structure of v_{Lk1u0} in the shoal in Case 2.
551 Stratification mainly affects the structure of v_{Lk1u0} in the lower layer of the deep channel. During

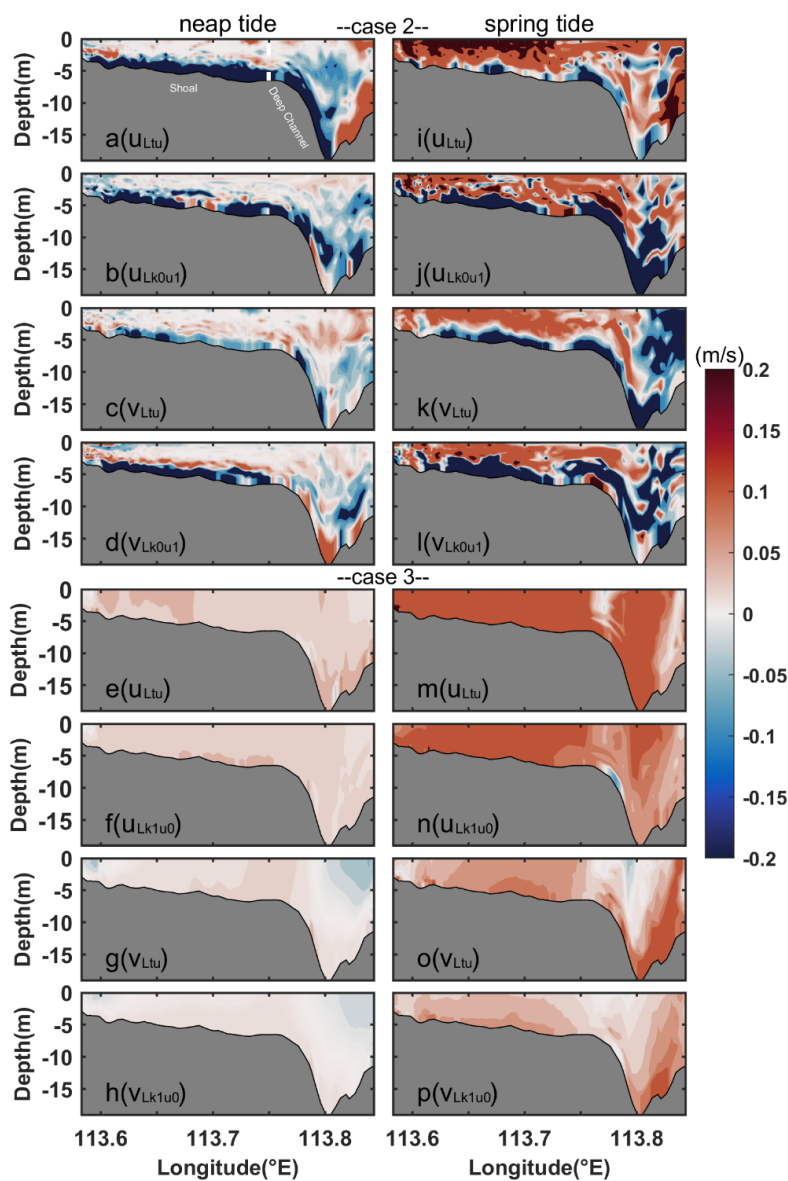


552 spring tides, the inflow area of v_{Lk1u0} for Case 3 in the deep channel is larger than that during
 553 neap tides (Fig. 14p). During both neap and spring tides, the u_{Ltu} and v_{Ltu} (Figs. 14e, g, m, and
 554 o) align with u_{Lk1u0} and v_{Lk1u0} (Figs. 14f, h, n, and p), respectively. Hence, u_{Ltu} and v_{Ltu} are
 555 primarily influenced by u_{Lk1u0} and v_{Lk1u0} , differing from the dominant components in Case 2.
 556 Without consideration of stratification, the dominant components of u_{Ltu} and v_{Ltu} shift from the
 557 turbulent mean components (u_{Lk0u1} and v_{Lk0u1}) in Case 2 to the tidal straining components (u_{Lk1u0}
 558 and v_{Lk1u0}) in Case 3. During neap tides, the magnitude of u_{Lk1u0} is approximately 5 times
 559 smaller than that in Case 2, while the magnitude of v_{Lk1u0} is around 14 times smaller than that
 560 in Case 2 (Table 3). During spring tides, the magnitude of u_{Lk1u0} is roughly 4 times smaller than
 561 that in Case 2, and the magnitude of v_{Lk1u0} is approximately 6 times smaller than that in Case
 562 2.

563 **Table 3.** The contribution of each component to the total eddy viscosity component in three scenarios.

	Case 1	Case 1	Case 2	Case 2	Case 3	Case 3
	(neap)	(spring)	(neap)	(spring)	(neap)	(spring)
$M(u_{Lk0u0})$	0.16	0.42	0.14	0.42	0.001	0.068
$M(u_{Lk0u1})$	0.11	0.27	0.07	0.20	0.006	0.010
$M(u_{Lk1u0})$	0.16	0.46	0.14	0.43	0.031	0.103
$M(u_{Lk1u1})$	0.08	0.17	0.04	0.16	0.001	0.003
$M(v_{Lk0u0})$	0.15	0.30	0.11	0.28	0.005	0.023
$M(v_{Lk0u1})$	0.11	0.19	0.07	0.15	0.011	0.032
$M(v_{Lk1u0})$	0.16	0.37	0.11	0.28	0.008	0.044
$M(v_{Lk1u1})$	0.11	0.20	0.05	0.13	0.001	0.004

564



565

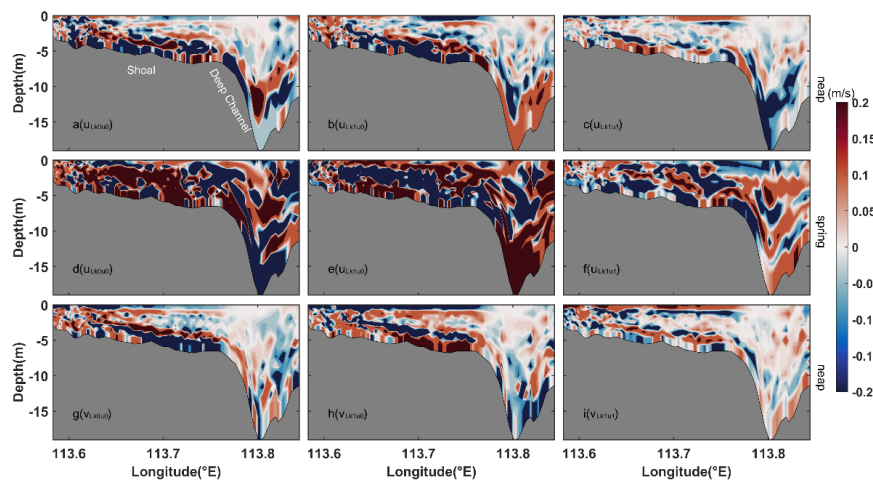
566 **Figure 14.** The structure of cross-estuary (u_{Ltu}) and along-estuary (v_{Ltu}) eddy viscosity components and the
 567 corresponding dominant components for Case 2 (a–d and i–l) and 3 (e–h, and m–p). Red shading represents
 568 eastward flow and blue shading represents westward flow for cross-estuary components. For along-estuary
 569 components, red shading represents inflow and blue shading represents outflow. The left column is for neap
 570 tides, and the right column is for spring tides.



571 **3.4 Contributions of non-dominant components for eddy viscosity component**

572 During neap tides, the cross-estuary coupled component of the tidal-averaged eddy
573 viscosity and velocity gradient oscillation (u_{Lk0u0}) for Case 1 demonstrates a vertically sheared
574 structure in the shoal, with alternating westward and eastward flows (Fig. 15a). During spring
575 tides, u_{Lk0u0} for Case 1 predominantly flows eastward in the shoal and displays a two-layer
576 structure in the deep channel with eastward flow in the upper layer and westward flow in the
577 lower layer (Fig. 15d). The cross-estuary tidal straining component (u_{Lk1u0}) during neap tides
578 exhibits an opposing structure to that of u_{Lk0u0} in the lower layer (Fig. 15b). In the upper layer,
579 it displays a similar pattern to u_{Lk0u0} . During spring tides, the extent and magnitude of the
580 eastward flow of u_{Lk1u0} in the deep channel are larger than during neap tides (Fig. 15e). During
581 neap tides, the cross-estuary coupled component of the eddy viscosity oscillation and the tidal-
582 averaged velocity gradient (u_{Lk1u1}) exhibits a complex vertically sheared structure (Fig. 15c).
583 During spring tides, u_{Lk1u1} displays a similar structure but with a greater magnitude than that
584 during neap tides (Fig. 15f). The combined effect of the three components, namely u_{Lk0u0} , u_{Lk1u0} ,
585 and u_{Lk1u1} , contrasts with u_{Lk0u1} .

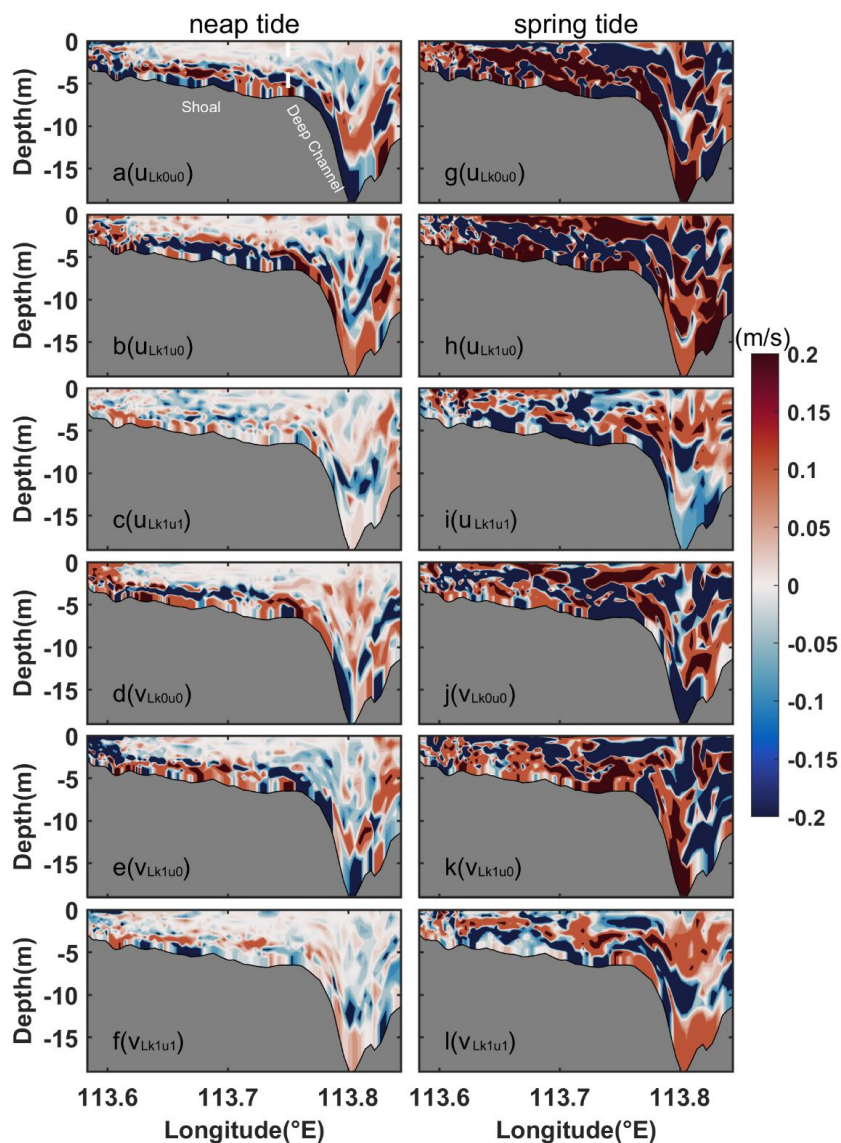
586 During neap tides, the along-estuary coupled component of the tidal-averaged eddy
587 viscosity and velocity gradient oscillation (v_{Lk0u0}) exhibits a vertically sheared structure with
588 alternating outflow and inflow in Case 1 (Fig. 15g). The structure of the along-estuary tidal
589 straining component (v_{Lk1u0}) closely resembles that of v_{Lk0u0} in the upper layer of the shoal,
590 while it is opposite in the lower layer of the shoal and deep channel (Fig. 15h). Additionally,
591 the cross-estuary coupled component of the eddy viscosity oscillation and the tidal-average
592 velocity gradient (v_{Lk1u1}) displays an opposite pattern to v_{Lk0u0} in the upper layer of the shoal
593 (Fig. 15i). The combined effects of the three along-estuary non-dominant components are
594 opposite to the dominant component (v_{Lk0u1}) and exert a negative contribution to the total eddy
595 viscosity component.



596

597 **Figure 15.** The structure of each non-dominant component of u_{Ltu} during neap tides (a–c) and spring tides
598 (d–f) for Case 1. Red shading represents eastward flow and blue shading represents westward flow. The
599 counterparts for v_{Ltu} during neap tides (g–i), in which red shading represents inflow and blue shading
600 represents outflow.

601 Without the wind forcing, the structure (Fig. 16) and magnitude (Table 3) of the non-
602 dominant components of the eddy viscosity component in Case 2 remain consistent with those
603 in Case 1 throughout the entire cross section. However, during neap tides, their magnitudes in
604 the upper layer are approximately one order of magnitude smaller compared to Case 1 (Figs.
605 16a–f), suggesting that wind has a significant effect on these subcomponents during relatively
606 small tides. During spring tides, both the structure (Figs. 16g–l) and magnitude (Table 3) of
607 each non-dominant component of the eddy viscosity component align with those in Case 1.
608 This suggests a weak influence of wind on the non-dominant components during spring tides.



609

610 **Figure 16.** The structure of each non-dominant component of u_{Ltu} and v_{Ltu} during neap tides (a–f) and spring
 611 tides (g–l) for Case 2. Red shading represents eastward flow and blue shading represents westward flow for
 612 the cross-estuary component. For the along-estuary component, red shading represents inflow and blue
 613 shading represents outflow.

614

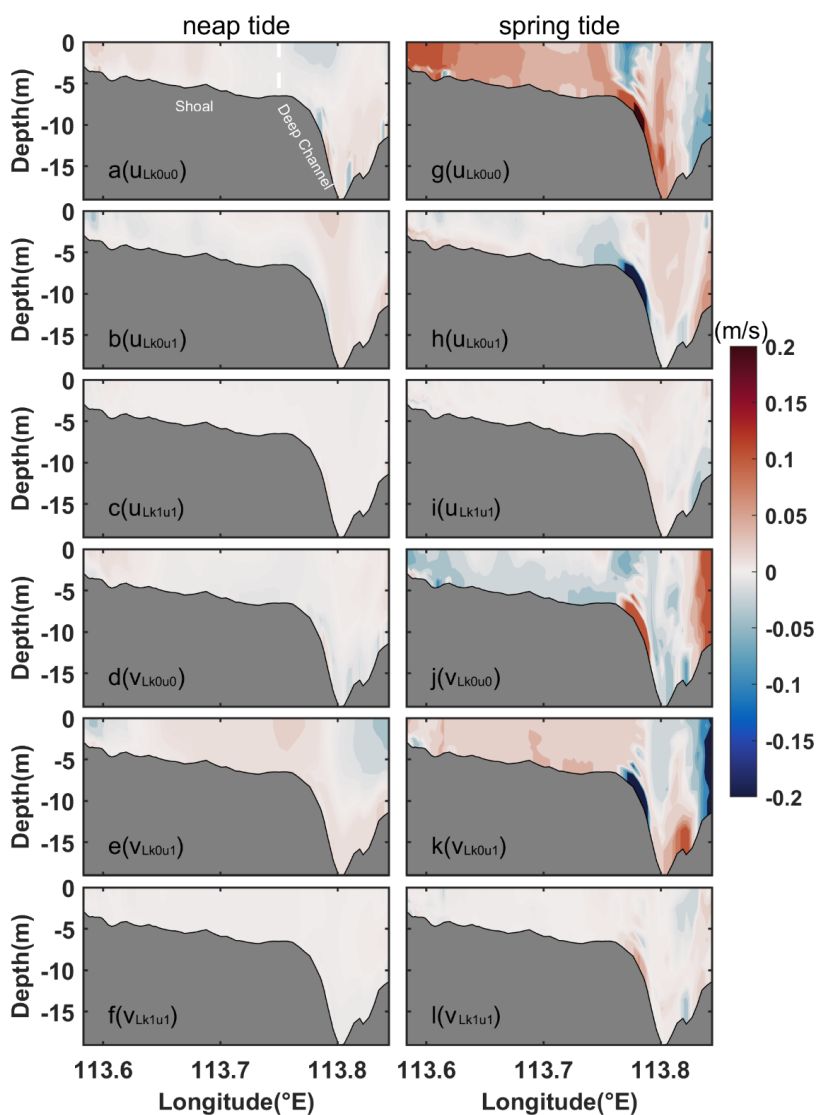


615 When stratification is further ignored in Case 3, the cross-estuary coupled component of
616 the tidal-averaged eddy viscosity and velocity gradient oscillation (u_{Lk0u0}) exhibits eastward
617 flow in the shoal and the lower layer of the deep channel, while displaying westward flow in
618 the upper layer of the deep channel during neap tides (Fig. 17a). This structure differs from that
619 in Case 2, and the magnitude of u_{Lk0u0} is approximately 14 times smaller than that in Case 2
620 (Table 3). The cross-estuary turbulent mean component (u_{Lk0u1}) for Case 3 predominantly flows
621 westward in most of the shoal, and eastward in most of the deep channel (Fig. 17b). The u_{Lk0u1}
622 transitions from westward flow in Case 2 to eastward flow in Case 3 in the lower layer of the
623 deep channel. Furthermore, the magnitude of u_{Lk0u1} in Case 3 is approximately 12 times smaller
624 than that in Case 2. During spring tides, the area of eastward flow of u_{Lk0u0} in the shoal is larger
625 than that observed during neap tides in Case 3 (Fig. 17g), and its magnitude is approximately
626 6 times smaller than that in Case 2. The structure of u_{Lk0u1} during spring tides aligns with that
627 observed during neap tides (Fig. 17h), while its magnitude is roughly 20 times smaller than
628 that in Case 2. The magnitude of the cross-estuary coupled component of eddy viscosity
629 oscillation and tidal-average velocity gradient (u_{Lk1u1}) (Figs. 17c and i) in Case 3 is the smallest
630 among the components (Table 3), ranging from 40 to 50 times smaller than that in Case 2.

631 The along-estuary non-dominant eddy viscosity subcomponents for Case 3 are depicted
632 in Figs. 17d–f and j–l. During neap tides, both the along-estuary coupled component of the
633 tidal-averaged eddy viscosity and velocity gradient oscillation (v_{Lk0u0}) and the along-estuary
634 coupled component of eddy viscosity oscillation and tidal-average velocity gradient (v_{Lk1u1})
635 exhibit horizontally sheared structures (Figs. 17d and f) that differ from those in Case 2. The
636 magnitudes of v_{Lk0u0} and v_{Lk1u1} are approximately 22–50 times smaller than those in Case 2
637 (Table 3). During spring tides, the structures of v_{Lk0u0} and v_{Lk1u1} (Figs. 17j and l) are relatively
638 similar to those during neap tides, and their magnitudes are approximately 12–32 times smaller



639 compared to Case 2. During neap tides, the along-estuary turbulent mean component (v_{Lk0ul})
640 for Case 3 displays inflow in the shoal and the lower layer of the deep channel, as well as
641 outflow in the upper layer of the deep channel (Fig. 17e). This pattern is opposite to that in
642 Case 2, and the magnitude of v_{Lk0ul} is approximately 14 times smaller than that in Case 2.
643 During spring tides, the outflow area of v_{Lk0ul} for Case 3 in the deep channel is larger than that
644 during neap tides (Fig. 17k), and the magnitude is approximately 5 times smaller than that in
645 Case 2. The results demonstrate the significant impact of stratification on each non-dominant
646 component of the eddy viscosity component.



647

648 **Figure 17.** Vertical section of each non-dominant component of u_{Ltu} and v_{Ltu} during neap tides (a–f) and
 649 spring tides (g–l) for Case 3. Red shading represents eastward flow and blue shading represents westward
 650 flow for cross-estuary components. For the along-estuary component, red shading represents inflow, and
 651 blue shading represents outflow.

652



653 **4. Discussion**

654 Several dimensionless parameters are examined to quantify the relative impact of the two
655 distinct forcings, respectively. The $K = \zeta_c / h_c$ is a parameter utilized to measure the intensity of
656 advection nonlinearity in the system (Jiang and Feng, 2014), where ζ_c and h_c are the
657 characteristic values of the tidal amplitude and depth, respectively. In most regions of the PRE,
658 the values of K are below 0.2, indicating relatively weak advection nonlinearity. Nonetheless,
659 in proximity to the shorelines, K surpasses 0.4 and can even approach 1 due to the shallow
660 topography, which suggests strong advection nonlinearity in nearshore regions of the PRE. The
661 selected regions for the four cross sections in this paper pertain to the relatively weakly
662 nonlinear zone, thus the LRV displays insensitivity to the initial release phase. The Peclet
663 number (Pe), defined as $u_c L_c / \nu_{Dc}$, measures the relative contribution between the nonlinear
664 advection and horizontal diffusion, where u_c , L_c , and ν_{Dc} are the scales of tidal current, the
665 estuary length, and the horizontal diffusion coefficient. The Pe for the PRE domain is several
666 orders of magnitude larger than 1 indicating horizontal diffusion is so small that it can be
667 ignored. The results in the paper have suggested the contribution of the horizontal diffusion
668 component is significantly lower than other components. Among all terms, the barotropic
669 pressure gradient has the largest scale, making the barotropic pressure gradient component of
670 LRV contribute the most compared to other components. The Wedderburn number (W) is
671 calculated to measure the contribution ratio of wind forcing to the baroclinic pressure gradient,
672 defined as $W = L_c T_w / (g \Delta \rho H_c^2)$ (Lange and Burchard, 2019). The value of W in the PRE is
673 0.0294 during neap tides and 0.0447, suggesting the baroclinic effects dominate in periodically
674 stratified waters and small W inhibits along-estuary gravitational circulation, which is identical
675 to that in Lange and Burchard (2019). The Simpson number (Si) is a parameter used to quantify
676 the level of stratification in estuaries (Simpson et al., 1990). It is calculated using the following
677 formula:



$$Si = \frac{\partial_x b H^2}{u_{max}^2}, \quad (8)$$

678 where $\partial_x b$ represents the tidal mean horizontal density gradient, H represents the water depth,
679 and u_{max} represents the absolute magnitude of the velocity amplitude. Based on the Simpson
680 number values, different stratification conditions can be determined for the estuary. The estuary
681 is categorized as well-mixed when $Si < 0.088$; In the case of $0.088 < Si < 0.84$, the estuary
682 displays periodic stratification; For $Si > 0.84$, the estuary is strongly stratified, as indicated by
683 Becherer et al. (2011). The Si for the PRE ranges from 0.1 to 0.45 in stratified conditions in
684 Cases 1 and 2, indicating that the estuary is periodically stratified. Sections B–D are arranged
685 in a north-to-south distribution, gradually approaching the open sea. The Si progressively
686 increases towards the open sea, with values ranging from 0.1 to 0.4 during neap tides and 0.05
687 to 0.1 during spring tides. This indicates that the magnitude of tides has substantial influences
688 on Si . With the increment in Si , the relative contributions of the tidal straining component and
689 the baroclinic pressure gradient component diminish. These findings align with those of Cheng
690 et al. (2011). Forced by wind, the relative contribution of the two components changes from 2
691 to 0.57 during neap tides and 2 to 1.4 during spring tides. However, in the absence of wind, the
692 relative contribution varies from 0.67 to 0.26 during neap tides and 1.4 to 0.9 during spring
693 tides, where the value of Si closely mirrors those with wind forcing. These results emphasize
694 the significant influence of the southwesterly wind on the relative contribution of these
695 components.

696 According to the Eulerian mean theory, the coupled component of tidal-averaged eddy
697 viscosity and velocity gradient oscillation (u_{Ek0u0}), and the coupled component of tidal-
698 averaged velocity gradient and eddy viscosity oscillation (u_{Ek1u1}) are zero (Burchard and
699 Hetland, 2010), however, in the Lagrangian mean theory, those components are not zero and
700 their magnitudes are comparable to other components under most conditions. Although the



701 tidal straining component of ERV has been extensively discussed, the contribution of the
702 turbulent mean term to the total ERV has not been analyzed in previous studies (Burchard and
703 Hetland, 2010; Burchard et al., 2011). This paper further analyzes the contribution from the
704 turbulent mean component of the LRV, in which the tidal mean component predominates the
705 eddy viscosity component under stratified conditions, and the tidal straining component plays
706 a significant role in the eddy viscosity component under homogeneous conditions.

707 The relevance of the Lagrangian residual circulation for mass transport in estuaries or
708 bays is evident. In the Eulerian-averaged salinity balance equation, a tidal dispersion term
709 emerges (Hansen and Rattray, 1965). This tidal dispersion term exhibits different dynamic
710 mechanisms in various estuaries (Fischer, 1976), and even within different sections of the same
711 estuary. However, when the isohaline averaging method is employed to quantitatively assess
712 estuarine circulation, the tidal dispersion term vanishes (MacCready, 2011; MacCready et al.,
713 2018; Wang et al., 2017). Nevertheless, the salinity coordinate method is only an approximate
714 Lagrangian approach. Future studies focusing on the dynamic mechanisms of salinity transport
715 from a Lagrangian averaging perspective will provide further insights into the subject.

716 **5. Conclusions**

717 This paper utilizes the FVCOM model to construct a hydrodynamic model in the PRE.
718 The model simulation results are validated using observed data, and the numerical model is
719 then employed to investigate the dynamic mechanism of the LRV in the estuary. By
720 quantitatively analyzing the contribution of each dynamic component to the LRV, the primary
721 mechanisms governing the LRV in the PRE under various dynamic conditions are elucidated.
722 Furthermore, to explore the influence of the eddy viscosity component on the LRV, it is
723 decomposed into four subcomponents and the contribution of each subcomponent is quantified.
724 This analysis reveals the dominant mechanism controlling the structure of the eddy viscosity



725 component under different dynamic conditions.

726 In the reference case, the cross-estuary LRV (u_L) exhibits a two-layer vertical structure
727 with eastward flow in the upper layer and westward flow in the lower layer. The two-layer
728 structure is primarily determined by the combined effects of the eddy viscosity component
729 (u_{Ltu}), the barotropic pressure gradient component (u_{Lba}), and the baroclinic pressure gradient
730 component (u_{Lgr}). The u_{Ltu} is the main contributor to the eastward flow in the upper layer of the
731 shoal, and u_{Lba} determines the eastward flow in the upper layer of the deep channel. For the
732 entire lower layer, the westward flow is dominated by u_{Ltu} and u_{Lba} , with u_{Lgr} playing a
733 balancing role. The along-estuary LRV (v_L) exhibits a two-layer gravitational circulation
734 pattern. The v_L is predominantly influenced by the imbalance of the barotropic pressure
735 gradient component (v_{Lba}) and the baroclinic pressure gradient component (v_{Lgr}). The outflow
736 is mainly dominated by v_{Lba} in the upper layer, while the inflow is primarily driven by v_{Lgr} in
737 the lower layer. For non-dominant components, the combined effects of the local acceleration
738 component, and the horizontal and vertical nonlinear component contributes less to total LRV.
739 The contribution of the horizontal diffusion component is negligible.

740 Without wind forcing, the eastward flow dominated by the eddy viscosity component (u_{Ltu})
741 transforms into the westward flow dominated by the barotropic pressure gradient component
742 (u_{Lba}) in the upper 2 m of the shoal. In other regions, the dominant components of the cross-
743 estuary LRV (u_L) roughly remain the same as those in the reference case, indicating that wind
744 mainly affects u_L in the upper layer by influencing u_{Ltu} . The structure and dominant components
745 of the along-estuary LRV (v_L) are nearly consistent with those in the reference case except for
746 some regions in the shoal, but the magnitude of the dominant components is larger than that in
747 the reference case, indicating that the southwesterly wind inhibits the along-estuary
748 gravitational circulation. The non-dominant components show no significant changes without
749 wind forcing, except for the along-estuary eddy viscosity component, which exhibits a reverse



750 structure in the upper layer compared to that with wind forcing.

751 Under unstratified conditions, the cross-estuary and along-estuary LRV (u_L , v_L) are
 752 transformed from the vertical shear structure in stratified waters to the lateral shear structure.
 753 The u_L is dominated by the sum of the local acceleration component (u_{Lac}), horizontal nonlinear
 754 component (u_{Ladh}), barotropic pressure gradient component (u_{Lba}), and eddy viscosity
 755 component (u_{Ltu}). The v_L is dominated by the sum of the barotropic pressure gradient
 756 component (v_{Lba}) and eddy viscosity component (v_{Ltu}), indicating that stratification
 757 significantly affects the structure and dominant components of the LRV.

758 This study highlights that the eddy viscosity component remains dominant regardless of
 759 the presence of stratification. Specifically, under stratified conditions, the turbulent mean
 760 component plays a dominant role in the total eddy viscosity component. Conversely, under
 761 unstratified conditions, the tidal straining component takes precedence over other factors in
 762 contribution to the total eddy viscosity component. The combined effects of non-dominant
 763 components have a negative contribution to the total eddy viscosity component.

764 Appendix

765 Numerical solutions of each component of the Lagrangian Residual Velocity (LRV)

766 Each term in the momentum equations is integrated along the particle trajectories over a
 767 tidal period and divided by the tidal period to obtain each dynamic component of Lagrangian
 768 residual velocity.

$$\begin{aligned}
 v_L = & \underbrace{\left\langle \frac{\partial u D}{D \partial t} \right\rangle / f}_1 + \underbrace{\left\langle \frac{\partial u^2 D}{D \partial x} + \frac{\partial uv D}{D \partial y} \right\rangle / f}_2 + \underbrace{\left\langle \frac{\partial u \omega D}{D \partial \sigma} \right\rangle / f}_3 + \underbrace{\left\langle g \frac{\partial \zeta}{\partial x} \right\rangle / f}_4 \\
 & - \underbrace{\left\langle \frac{1}{D^2} \frac{\partial}{\partial \sigma} \left(v_h \frac{\partial u}{\partial \sigma} \right) \right\rangle / f}_5 + \underbrace{\left\langle \frac{g}{\rho_0} \left(D \int_{\sigma}^0 \frac{\partial \rho}{\partial x} d\sigma_1 + \frac{\partial D}{\partial x} \int_{\sigma}^0 \sigma_1 \frac{\partial \rho}{\partial \sigma_1} d\sigma_1 \right) \right\rangle / f}_6 - \underbrace{\langle E_x \rangle / f}_7, \quad (A1)
 \end{aligned}$$



$$\begin{aligned}
 u_L = & \underbrace{-\left\langle \frac{\partial v D}{D \partial t} \right\rangle / f}_1 - \underbrace{\left\langle \left(\frac{\partial u v D}{D \partial x} + \frac{\partial v^2 D}{D \partial y} \right) \right\rangle / f}_2 - \underbrace{\left\langle \frac{\partial v \omega D}{D \partial \sigma} \right\rangle / f}_3 - \underbrace{\left\langle g \frac{\partial \zeta}{\partial y} \right\rangle / f}_4 \\
 & + \underbrace{\left\langle \frac{1}{D^2} \frac{\partial}{\partial \sigma} \left(v_h \frac{\partial v}{\partial \sigma} \right) \right\rangle / f}_5 - \underbrace{\left\langle \frac{g}{\rho_0} \left(D \int_{\sigma}^0 \frac{\partial \rho}{\partial y} d\sigma_1 + \frac{\partial D}{\partial y} \int_{\sigma}^0 \sigma_1 \frac{\partial \rho}{\partial \sigma_1} d\sigma_1 \right) \right\rangle / f}_6 + \underbrace{\left\langle F_y \right\rangle / f}_7, \quad (A2)
 \end{aligned}$$

769 where $u(x, y, \sigma, t)$, $v(x, y, \sigma, t)$, and $\omega(x, y, \sigma, t)$ represent velocity components in the
 770 longitudinal (x), latitudinal (y), and vertical (σ) directions, respectively. The $\rho(x, y, \sigma, t)$ is
 771 water density, ρ_0 is the reference density, t is the time, f is the Coriolis parameter, and $v_h(x, y,$
 772 $\sigma, t)$ is eddy viscosity coefficient. The $D = H + \zeta$, where $H(x, y)$ is the water mean depth, $\zeta(x, y,$
 773 $t)$ is the water surface elevation. The first term refers to local acceleration component, the
 774 second terms represent horizontal nonlinear advection components, the third term depicts the
 775 nonlinear vertical advection component, the fourth term corresponds to the barotropic pressure
 776 gradient component, the fifth term describes the eddy viscosity component, the sixth terms
 777 denote the baroclinic pressure gradient components, and the seventh term pertains to horizontal
 778 diffusion component. The $\langle \rangle$ denotes the Lagrangian mean operator.

779 Data availability

780 Hydrodynamic datasets used in this study are available online at
 781 <https://doi.org/10.5281/zenodo.8323286> (Deng et al., 2023). The 1° World Ocean Atlas 2009
 782 (WOA2009) datasets are accessible online from (<https://accession.nodc.noaa.gov/0094866>).
 783 The 0.25° CCMP datasets are available online (<http://www.remss.com/measurements/ccmp>).
 784 The monthly average river runoff data are provided by the Water Conservancy Committee of
 785 the Pearl River under the Ministry of Water Resources. The topography data off the PRE are
 786 from the ETOPO2 dataset of NOAA
 787 (<https://www.ngdc.noaa.gov/mgg/global/relief/ETOPO2/ETOPO2v2-2006/>), while those
 788 within the estuary are provided by the China Maritime Safety Administration.

789 Author contributions



790 All authors have contributed to the conceptualization and design of this study. The
791 analytical methods were originally formulated by FD. Subsequently, FD and ZC meticulously
792 processed and analyzed the data. The model was collaboratively developed and the manuscript
793 was co-authored by FD, FJ, and ZC. The final manuscript underwent a thorough review and
794 editing process, led by RS, SZ, QL, and XZ, ensuring its quality and accuracy.

795 **Competing interests**

796 The contact author has declared that none of the authors has any competing interests.

797 **Acknowledgments**

798 This study was supported by the National Natural Science Foundation of China (Grants
799 41906144, 42276013, 92158201, 42106028, and 42206028), the State Key Laboratory of
800 Tropical Oceanography, South China Sea Institute of Oceanology, Chinese Academy of
801 Sciences (Project No. LTO2318), and the Innovation and Entrepreneurship Project of Shantou
802 (Grant 201112176541391).

803 **References**

804 Becherer, J., Burchard, H., Flöser, G., Mohrholz, V., Umlauf, L.: Evidence of tidal straining in
805 well-mixed channel flow from micro-structure observations, *Geophys. Res. Lett.*, 38(17),
806 <https://doi.org/10.1029/2011GL049005>, 2011.

807 Burchard, H., Hetland, R. D., Schulz, E., Schuttelaars, H. M.: Drivers of residual estuarine
808 circulation in tidally energetic estuaries: Straight and irrotational channels with parabolic
809 cross section, *J. Phys. Oceanogr.*, 41(3), 548–570, <https://doi.org/10.1175/2010JPO4453.1>,
810 2011.

811 Burchard, H., Hetland, R. D.: Quantifying the contributions of tidal straining and gravitational
812 circulation to residual circulation in periodically stratified tidal estuaries, *J. Phys. Oceanogr.*,
813 40(6), 1243–1262, <https://doi.org/10.1175/2010JPO4270.1>, 2010.



- 814 Burchard, H.: Combined effects of wind, tide and horizontal density gradients on stratification
815 in estuaries and coastal seas, *J. Phys. Oceanogr.*, 39, 2117–2136,
816 <https://doi.org/10.1175/2009JPO4142.1>, 2009.
- 817 Chen, Y., Cui, Y. X., Sheng, X. X., Jiang, W. S., Feng, S. Z.: Analytical solution to the 3D tide-
818 induced Lagrangian residual current in a narrow bay with vertically varying eddy viscosity
819 coefficient, *Ocean Dyn.*, 70, 759–770, <https://doi.org/10.1007/s10236-020-01359-3>, 2020.
- 820 Cheng, P., Valle-Levinson, A., de Swart, H. E.: A numerical study of residual circulation
821 induced by asymmetric tidal mixing in tidally dominated estuaries, *J. Geophys. Res.:
822 Oceans*, 116(C1), <https://doi.org/10.1029/2010JC006137>, 2011.
- 823 Chu, N. Y., Liu, G. L., Xu, J., Yao, P., Du, Y., Liu, Z. Q., Cai, Z. Y.: Hydrodynamical transport
824 structure and lagrangian connectivity of circulations in the Pearl River Estuary, *Front. Mar.
825 Sci.*, 9, 996551, <https://doi.org/10.3389/fmars.2022.996551>, 2022.
- 826 Cui, Y. X., Jiang, W. S., Deng, F. J.: 3D numerical computation of the tidally induced
827 Lagrangian residual current in an idealized bay, *Ocean Dyn.*, 69, 283–300,
828 <https://doi.org/10.1007/s10236-018-01243-1>, 2019.
- 829 Deng, F. J., Jiang, W. S., Feng, S. Z.: The nonlinear effects of the eddy viscosity and the bottom
830 friction on the Lagrangian residual velocity in a narrow model bay, *Ocean Dyn.*, 67, 1105–
831 1118, <https://doi.org/10.1007/s10236-017-1076-x>, 2017.
- 832 Deng, F. J., Jiang, W. S., Valle-Levinson, A., Feng, S. Z.: 3D modal solution for tidally induced
833 Lagrangian residual velocity with variations in eddy viscosity and bathymetry in a narrow
834 model bay, *J. Ocean Univ. China*, 18, 69–79, <https://doi.org/10.1007/s11802-019-3773-1>,
835 2019.



- 836 Deng, F. J., Jiang, W. S., Zong, X. L., Chen, Z. Y.: Quantifying the Contribution of Each Driving
837 Force to the Lagrangian Residual Velocity in Xiangshan Bay, *Front. Mar. Sci.*, 9, 901490,
838 <https://doi.org/10.3389/fmars.2022.901490>, 2022.
- 839 Feng, S. Z.: A three-dimensional weakly nonlinear model of tide-induced Lagrangian residual
840 current and mass-transport, with an application to the Bohai Sea, *Elsevier Oceanogr. Ser.*,
841 45, 471–488, [https://doi.org/10.1016/S0422-9894\(08\)70463-X](https://doi.org/10.1016/S0422-9894(08)70463-X), 1987.
- 842 Feng, S. Z., Xi, P. G., Zhang, S. Z.: The baroclinic residual circulation in shallow seas: I. The
843 hydrodynamic models, *Chin. J. Oceanol. Limnol.*, 2, 49–60,
844 <https://doi.org/10.1007/BF02888391>, 1984.
- 845 Fischer, H. B., List, J., Koh, C. R., Imberger, J., Brooks, N. H.: *Mixing in inland and coastal*
846 *waters*, Academic Press, <https://doi.org/10.1016/C2009-0-22051-4>, 1979.
- 847 Geyer, W. R., MacCready, P.: The estuarine circulation, *Annu. Rev. Fluid Mech.*, 46, 175–197,
848 <https://doi.org/10.1146/annurev-fluid-010313-141302>, 2014.
- 849 Gong, W. P., Lin, Z. Y., Chen, Y. Z., Chen, Z. Y., Zhang, H.: Effect of winds and waves on salt
850 intrusion in the Pearl River estuary, *Ocean Sci.*, 14(1), 139–159, [https://doi.org/10.5194/os-](https://doi.org/10.5194/os-14-139-2018)
851 [14-139-2018](https://doi.org/10.5194/os-14-139-2018), 2018.
- 852 Hansen, D. V., Rattray, M.: Gravitational circulation in straits and estuaries, *J. Mar. Res.*, 79(2),
853 69–87, <https://doi.org/10.1357/002224021834614399>, 1965.
- 854 Ianniello, J. P.: Tidally induced residual currents in estuaries of constant breadth and depth, *J.*
855 *Mar. Res.*, 9(5), 962–974, 1977.
- 856 Jay, D. A., Musiak, J. D.: Particle trapping in estuarine tidal flows, *J. Geophys. Res.: Oceans*,
857 99(C10), 20445–20461, <https://doi.org/10.1029/94JC00971>, 1994.



- 858 Jiang, W. S., Feng, S. Z.: 3D analytical solution to the tidally induced Lagrangian residual
859 current equations in a narrow bay, *Ocean Dyn.*, 64, 1073–1091,
860 <https://doi.org/10.1007/s10236-014-0738-1>, 2014.
- 861 Jiang, W. S., Feng, S. Z.: Analytical solution for the tidally induced Lagrangian residual current
862 in a narrow bay, *Ocean Dyn.*, 61, 543–558, <https://doi.org/10.1007/s10236-011-0381-z>,
863 2011.
- 864 Jongbloed, H., Schuttelaars, H. M., Dijkstra, Y. M., Donkers, P. B., Hoitink, A. J.: Influence of
865 wind on subtidal salt intrusion and stratification in well-mixed and partially stratified
866 estuaries, *J. Phys. Oceanogr.*, 52(12), 3139–3158, [https://doi.org/10.1175/JPO-D-21-](https://doi.org/10.1175/JPO-D-21-0291.1)
867 0291.1, 2022.
- 868 Lai, W. F., Pan, J. Y., Devlin, A. T.: Impact of tides and winds on estuarine circulation in the
869 Pearl River Estuary, *Cont. Shelf Res.*, 168, 68–82,
870 <https://doi.org/10.1016/j.csr.2018.09.004>, 2018.
- 871 Lamb, H.: *Hydrodynamics*, London: Cambridge university press, 1975.
- 872 Lange, X., Burchard, H.: The relative importance of wind straining and gravitational forcing
873 in driving exchange flows in tidally energetic estuaries, *J. Phys. Oceanogr.*, 49(3), 723–736,
874 <https://doi.org/10.1175/JPO-D-18-0014.1>, 2019.
- 875 Liu, G. L., Liu, Z., Gao, H. W., Feng, S. Z.: Initial time dependence of wind-and density-driven
876 Lagrangian residual velocity in a tide-dominated bay, *Ocean Dyn.*, 71, 447–469,
877 <https://doi.org/10.1007/s10236-021-01447-y>, 2021.
- 878 MacCready, P.: Calculating estuarine exchange flow using isohaline coordinates, *J. Phys.*
879 *Oceanogr.*, 41, 1116–1124, <https://doi.org/10.1175/2011JPO4517.1>, 2011.



- 880 MacCready, P., Geyer, W. R., Burchard, H.: Estuarine exchange flow is related to mixing
881 through the salinity variance budget, *J. Phys. Oceanogr.*, 48, 1375–1384,
882 <https://doi.org/10.1175/JPO-D-17-0266.1>, 2018.
- 883 Monismith, S. G., Burau, J. R., Stacey, M.: Stratification dynamics and gravitational circulation
884 in northern San Francisco Bay, *San Francisco Bay: The Ecosystem*, 123, 153, 1996.
- 885 Pan, J. Y., Lai, W. F., Devlin, A. T.: Channel-Trapped Convergence and Divergence of Lateral
886 Velocity in the Pearl River Estuary: Influence of Along-Estuary Variations of Channel
887 Depth and Width, *J. Geophys. Res.: Oceans*, 125(1), e2019JC015369,
888 <https://doi.org/10.1029/2019JC015369>, 2020.
- 889 Pritchard, D. W.: Estuarine hydrography, *Adv. Geophys.*, 1, 243–280,
890 [https://doi.org/10.1016/S0065-2687\(08\)60208-3](https://doi.org/10.1016/S0065-2687(08)60208-3), 1952.
- 891 Pritchard, D. W.: The dynamic structure of a coastal plain estuary, *J. Mar. Res.*, 15(1), 33–42,
892 1956.
- 893 Quan, Q., Mao, X. Y., Jiang, W. S.: Numerical computation of the tidally induced Lagrangian
894 residual current in a model bay, *Ocean Dyn.*, 64, 471–486, [https://doi.org/10.1007/s10236-](https://doi.org/10.1007/s10236-014-0696-7)
895 [014-0696-7](https://doi.org/10.1007/s10236-014-0696-7), 2014.
- 896 Sheng, X. X., Mao, X. Y., Yu, J. Z., Zhang, X. Q., Jiang, W. S., Lu, Y. Y.: Modeling Lagrangian
897 residual velocity in a tide-dominated long-narrow bay: case study of the inner Xiangshan
898 Bay, *Estuar. Coast. Shelf Sci.*, 278, 108088, <https://doi.org/10.1016/j.ecss.2022.108088>,
899 2022.
- 900 Simpson, J. H., Brown, J., Matthews, J., Allen, G.: Tidal straining, density currents, and stirring
901 in the control of estuarine stratification, *Estuaries* 13, 125–132,
902 <https://doi.org/10.2307/1351581>, 1990.



- 903 Verspecht, F., Rippeth, T. P., Howarth, M. J., Souza, A. J., Simpson, J. H., Burchard, H.:
904 Processes impacting on stratification in a region of freshwater influence: Application to
905 Liverpool Bay, J. Geophys. Res.: Oceans, 114(C11),
906 <https://doi.org/10.1029/2009JC005475>, 2009.
- 907 Wang, B.: Analysis on the estuarine circulation and its dynamic mechanism in the
908 Lingdingyang Bay, Chinese Journal of Hydrodynamics, 29(05), 608–617, 2014.
- 909 Wang, J. H., Shen, Y. M., Guo, Y. K.: Seasonal circulation and influence factors of the Bohai
910 Sea: a numerical study based on Lagrangian particle tracking method, Ocean Dyn., 60,
911 1581–1596, <https://doi.org/10.1007/s10236-010-0346-7>, 2010.
- 912 Wang, T., Geyer, W. R., MacCready, P.: Total exchange flow, entrainment, and diffusive salt
913 flux in estuaries, J. Phys. Oceanogr., 47, 1205–1220, [https://doi.org/10.1175/JPO-D-16-](https://doi.org/10.1175/JPO-D-16-0258.1)
914 0258.1, 2017.
- 915 Wei, X. Y., Schuttelaars, H. M., Williams, M. E., Brown, J. M., Thorne, P. D., Amoudry, L. O.:
916 Unraveling interactions between asymmetric tidal turbulence, residual circulation, and
917 salinity dynamics in short, periodically weakly stratified estuaries, J. Phys. Oceanogr.,
918 51(5), 1395–1416, <https://doi.org/10.1175/JPO-D-20-0146.1>, 2021.
- 919 Wei, X. Y., Williams, M. E., Brown, J. M., Thorne, P. D., Amoudry, L. O.: Salt intrusion as a
920 function of estuary length in periodically weakly stratified estuaries, Geophys. Res. Lett.,
921 49(15), e2022GL099082, <https://doi.org/10.1029/2022GL099082>, 2022.
- 922 Winant, C. D.: Three-dimensional residual tidal circulation in an elongated, rotating basin, J.
923 Phys. Oceanogr., 38(6), 1278–1295, <https://doi.org/10.1175/2007JPO3819.1>, 2008.



- 924 Xu, H. Z., Shen, J., Wang, D. X., Luo, L., Hong, B.: Nonlinearity of subtidal estuarine
925 circulation in the Pearl River Estuary, China, *Front. Mar. Sci.*, 8, 629403,
926 <https://doi.org/10.3389/fmars.2021.629403>, 2021.
- 927 Xue, H. J., Chai, F., Wang, L. Y., Chen, J. Z.: *Zhujiang River Estuarine circulation model*, China
928 Ocean Press, 147–160, 2001.